2020

A Four-Port DC-DC Converter for a Hybrid Wind/Solar Energy System

Jiahong Ning
Minnesota State University, Mankato

A FOUR-PORT DC-DC CONVERTER FOR A HYBRID WIND/SOLAR ENERGY SYSTEM

by

Jiahong Ning

A THESIS

Presented to the Faculty of

The Graduate College at the Minnesota state

In Partial Fulfillment of Requirements

For the Degree of Master

Major: Electrical Engineering

Under the Supervision of Professor Jianwu Zeng

Minnesota State University, Mankato

July 2020

July 10, 2020

A Four-Port DC-DC converter for a hybrid wind/solar energy system, Jiahong Ning

This thesis has been examined and approved by the following members of the student's committee.

_____

Advisor

_____

Committee Member

_____

Committee Member

A FOUR-PORT DC-DC CONVERTER FOR A HYBRID WIND/SOLAR ENERGY SYSTEM

Jiahong Ning. M.S.

University of Minnesota State, Mankato, 2020

Advisor: Jianwu Zeng

With the increasing demand for clean and hybrid energy in the last decades, more and more attentions are paid to the renewable energy, e.g., wind and solar energy. According to the International Energy Agency, solar power was growing-fastest source in the world. In a hybrid wind/solar system, power converters play an important role in in power management and the voltage regulation. Gradually, power systems have undergone a paradigm shift from centralized generation to distributed generation. Smart grid, which is a combination of power systems and communication networks, was proposed to allow power systems to fit the future system challenge.

However, Due to their intermittence characteristics, energy storage such as battery is used together with renewable energy sources. Generally, there are two ways to integrate these distributed energy sources, one is to use several individual converters for each source; the other is to use an integrated multiple ports converter. The later

solution is preferable because some component can be shared and has lower cost and higher efficiency than that using several individual converters.

In this thesis, a new four-port DC-DC converter is proposed for a hybrid wind/solar energy system. The operation principle is analyzed and different controllers are designed to regulating the DC-link and source voltage, power management for the battery and maximum power point tracking (MPPT) for the renewable energy sources. The effectiveness of the hardware design and controllers are validated by a developed prototype which interfaces wind turbine generator, photovoltaic (PV) panel, battery, and the load.

ACKNOWLEDGMENTS

It is my honor to thank many of the people who have guided, helped, and encouraged me throughout my graduate school life at Minnesota State University, Mankato (MNSU).

First of all, I would like to express my sincere gratitude to my academic advisor, Dr. Jianwu Zeng, for allowing me to join his renewable energy research team and to attend various professional activities, for helping me to overcome difficulties regarding the changes of my study and research area, and for advising me in many of aspects both academic and in life. Thank you, Dr. Jianwu Zeng.

Then, I would like to thank my committee members: Dr. Vincent Winstead and Dr. Qiang Ye. Thanks for their time and effort to become one of my committee members, and for their constructive criticism. At the same time, I would also like to thank all faculty and staff from the Department of Electrical and Computer Engineering and Technology (ECET) at MNSU for their work hard, the useful suggestions, and comprehensive resources provided to all students.

Finally, I would like to thank my parents and my friends who have always accompanied me with their continuous encouragement and unfailing support. This accomplishment would not have been possible without any of you. Thank you.

Financial support from the Xcel Energy through a grant from the Renewable Development Fund is gratefully acknowledged.

TABLE OF CONTENTS

Chapter 1 Introduction 1

1.1 The background of the type of energy system 2

1.1.1 The power supply from the wind turbine generator 2

1.1.2 The solar power and PV panel 3

1.1.3 The microgrid system 4

1.2 The research actuality of multi-port DC-DC converter 5

1.2.1 The commonly used topologies of multiport DC converter 6

1.2.2 Controllers' logic of multiport DC/DC converter 8

Chapter 2 : The Literature of three-port DC converter Topology 11

2.1 Full-bridge three-port DC converter 11

2.2 The topology of full-bridge DC converter 13

2.3 The PWM controller logic of the full-bridge three-port DC converter . 14

2.4 The working principle of full-bridge DC converter 15

2.5 The advantage and disadvantage of full-bridge DC converter 17

Chapter 3 The system design of Four-port DC/DC converter 18

3.1 The system structure of the Four-Port DC Converter 18

3.2 The circuit parameter design of FPC 19

3.3 The design of high-frequency transformers 19

3.3.1 Drawing the Circuit Panel and Selection of Iron 20

3.3.2 The material choice of magnetic core and device 22

3.3.3 The structure of the magnetic core 23

3.3.4 Design of PCB 24

3.3.5 The transformer production 28

3.3.6 The leakage loss from the transformer test 28

3.4 Switching chosen of half-bridge in converter side 30

3.4.1 Introduction of the GaN material 30

3.4.2 The basic circuit structure of fast closed GaN device 31

3.5 The PCB layout circuit and schematic processing. 36

Chapter 4 ： The Working Principle of the Four-port DC/DC Converter 38

4.1 The working theory of Four-port DC converter's (FPC) topology.....38

4.2 FPC operation principle and analysis 41

4.3 The steady-state analysis of FDC's topology 44

4.4 The Controller design of the proposed converter 45

Chapter 5 Simulation and Experiment Verification.....49

5.1 Established of the Simulation Circuit System 49

5.2 Experient result 53

5.2.1 The Steady-State Waveforms 55

5.3 Transient response 57

5.4 The analysis of efficiency and voltage regulation 61

Chapter 6 Conclusion and Recommendation for Future Work 64

Bibliography 65

Appendix 71

LIST OF FIGURES

Fig. 1.1 The basic structure of Converter system 3

Fig. 1.2 The distribution of power source.....5

Fig. 1.3 Traditional half-bridge three-port DC converter. (a) originally …; (b) Secondary side adjustment three-port DC converter; (c) Secondary adjustment three-port DC converter (d)Buck-Boost full-bridge DC converter. 7

Fig. 1.4 Controller logic.....9

Fig. 2.1 Traditional full-bridge DC converter topology 12

Fig. 2.2 Dissymmetric full-bridge three-port DC converter 12

Fig. 2.3 A type of ZVZCS full-bridge Three-port DC converter's topology ..13

Fig. 2.4 Complementary conduction (a) Bipolar control method (b) finite unipolar control method(c) phase shift control method.....14

Fig. 2.5 Three port converter working mode(a)Single input and output (b)Double input and single-output (c) Single input and double output 16

Fig. 3.1 Four-port DC converter system block 18

Fig. 3.2 Classical transformer structure 20

Fig. 3.3 The Panel transformer physical transformer 21

Fig. 3.4 (a) Relationship between leakage, AC resistance and spacing (b) Power in isolation layer and thickness.....25

Fig. 3.5 Normally used kind of Crossing structure.....26

Fig. 3.6 The crossing-distribution about current density (f=500KHz) 27

Fig. 3.7 Current and leakage value in different combination 28

Fig. 3.8 Psychical transformer 29

Fig. 3.9 Altium design production 29

Fig. 3.10 The loss from the transformer in leakage and Iron.....30

Fig. 3.11 Package outline of GaN package(a)Package pad (b)Circuit figure..32

Fig. 3.12 GS66508T-Gate bias(a) and driver circuit (b)PMEG4010CEH.....34

Fig. 3.13 Secondary side of DC converter.....36

Fig. 3.14 Schematic page of converter board for reference.....37

Fig. 4.1 The over viewer of the Four-port DC-DC converter.....38

Fig. 4.2 Three-port phase-shift DC-DC converter.....40

Fig. 4.3 the proposed four-port DC-DC converter.....40

Fig. 4.4 Waveform changing with stage operation.....41

Fig. 4.5 Equivalent circuit of the different operation stage 43

Fig. 4.6 signal flows of the controllers and plant.....46

Fig. 4.7 Organization of controllers.....48

Fig. 5.1 Simple simulation graphic.....50

Fig. 5.2 Controller's wave graphic on simulation.....51

Fig. 5.3 Plus wide modulation signal while Phase shifting(a) $d = 0.5$ (b) $d = 0.6$

.....53

Fig. 5.4 Experiment Setup 54

Fig. 5.5 Steady-state waveform of i_{p1}, i_{p2}, and $v_{AB.}$ (a) charge mode(b) Discharge mode 55

Fig. 5.6 Measured ZVS of switches S2 and S4.....56

Fig. 5.7 simulation result Converter mode changing.....57

Fig. 5.8 Dynamic processing of switching while regular voltage was 91V 58

Fig. 5.9 Measured Waveforms during the mode transition in 180 V 61

Fig. 5.10 Voltage gain vs. duty cycle.....61

Fig. 5.11 Efficiency measure while charging mode and discharge mode 62

Fig. 5.12 Power of transformer's efficiency work in both mode (a) Charge mode (b) Discharge mode.....63

LIST OF TABLES

Table. 3.1 Parameters of FDC.....19

Table. 5.1 Parameter of component.....54

LIST OF Appendix

A. 1 Physical transformer(a) Side view (b)Overlook view.....71

A. 2 PCB layout schematic page.....72

Chapter 1 Introduction

With the global development of the economy and population, the energy dilemma is becoming more and more serious. There are several complex problems, for example, the traditional energy like fossil fuel not only brings the environmental damage and global warming critical incident, but also results in the shortage of energy due to this non-renewable energy source will be quickly consumed up in the future [7]. Furthermore, clean energy, including solar and wind energy, has been paid much attention to the industry. Which renewable system commonly includes the power system and storage system for the network unstable, discontinue problems. However, converters and energy storage system (ESS) with, stable and small size is desired. Multiport DC converter also can be applied in the renewable energy system and the electric vehicle with several different energy sources. Compared to those using an individual converter for each source, the multiport converter which combines several unidirectional/bidirectional converts, has the advantages of simple structure, lower cost, and higher efficiency [8].

Depending on the number of the ports [9], the multiport DC-DC converter can be classified into two types: three-port DC converter (TPC) and Four-port DC converter (FDC). By using a multiport DC-DC converter (MPC, the power management of ESS, solar panel, and load will be solved. Therefore, the application of the multiport converter which applies in the renewable energy system (RES) is not only helpful in power electronics research but also valuable in practical application.

Recently, there is so much advanced research about MDC topology, flexible branch switch, and control algorithm. The flexible branch switch technology was applied for reducing the switching loss, and the switching can be usually classified into two categories, the hard switching, and soft switching. With the increasing requirement of more efficient and higher switching frequency, hard switching cannot meet the requirement of power electronics development. Soft switching not only reduces or eliminates the switching loss, but also resolves the noise infection problem such as electromagnetic interference. In this situation, this kind of project will fit some middle or large power supply, like the EV supply system, ESS, and RES.

1.1 The background of the type of energy system

Renewable energy included wind, and solar power attracted much attention because of its clean and alternative characteristics. According to the International Energy Agency, solar power was the fastest-growing source of global energy recently [10]. And as solar tech development, the solar panel was widely accepted and commonly used in life and industries.

1.1.1 The power supply from the wind turbine generator

The wind turbine works in converting wind power to mechnical power, which takes rotor running and finally outputs AC power. The wind turbine unit was combined with generators, wind wheel, tail fin, and storage system, etc.

The basic theory of wind turbines is that the bald of the rotor utilizes wind power running and increasing by the growth of the engine, to generate electrical energy. The wind power has brought a kind of trend about hybrid energy because wind energy was clean energy and does not generate radiation or air pollution.

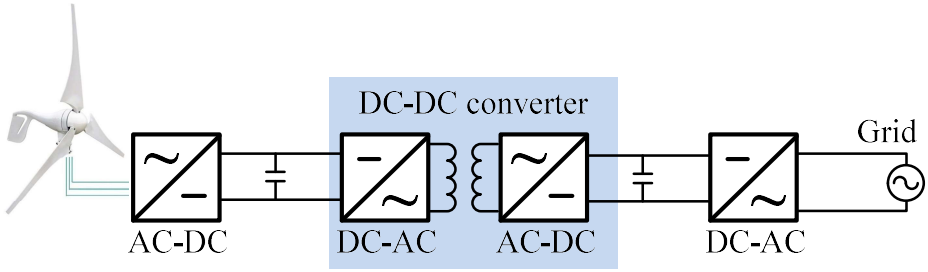

Fig. 1.1 The basic structure of Converter system

1.1.2 The solar power and PV panel

The solar energy system consists of a solar controller and solar battery storage pack. The solar power system is able to convert solar power to electrical power connected to the utility grid, which is widely used in a residential area in the U.S.

The solar power system is mainly divided into an off-grid generating system and grid-connected system, including a parallel generation system and distributed solar generator system. The Off-grid generating system mainly included a solar panel, battery pack, power converter with the controller, and load.

The parallel generation system is that solar power converted by an inverter to a public power grid. The character of the parallel generator system was that the electrical power directly transported to the big grid, and the manager unified deployment to the user. This kind of system cost large, longer building period and lower return on

investment. But the distribute small parallel solar power system has the advantage of small investment and fast return value, which was more popular.

Distributed solar generator system is small especially power system which server for some specific user or support the economic operation of the existing distributing power system, e.g., balance peak power system.

1.1.3 The microgrid system

The proposed implementation of micro-grid is to design to achieve the flexible and efficient application of distributed power supply, solve the problem of the large number, and various standards of distributed energy source in the processing of grid-connecting.

The micro-grid mainly includes DC-Micro-grid, AC-Micro-grid, and hybrid AC&DC-Microgrid. First, in the DC-Micro-grid, distribution energy sources, storage package, and load are connected to the DC bus which is connected to a large network by using the converter. It is the ease of adjusting the voltage level. And then, in AC-Micro-grid, the distributed energy source and storage machine are connected to the AC bus, which is the main form of a microgrid in nowadays. According to control the switching, the grid can switch between micro-grid mode and island mode.

In worldwide, many countries invest huge source in microgrids, e.g., Japan, as energy scarcity countries, pays more attention to energy diversity, reduces power pollution, and fills diversity requirements from users. The flexible and reliable intelligent system is put forward by Japanese researchers, aims to improve the power

system structure by adding some AC-device and controller to fill diversity power requirements.

From the world's view, the micro-grid [11] is in the experimental and demonstration stage. In the future, five or ten years, the scale of the micro-grid market will be further improved [12].

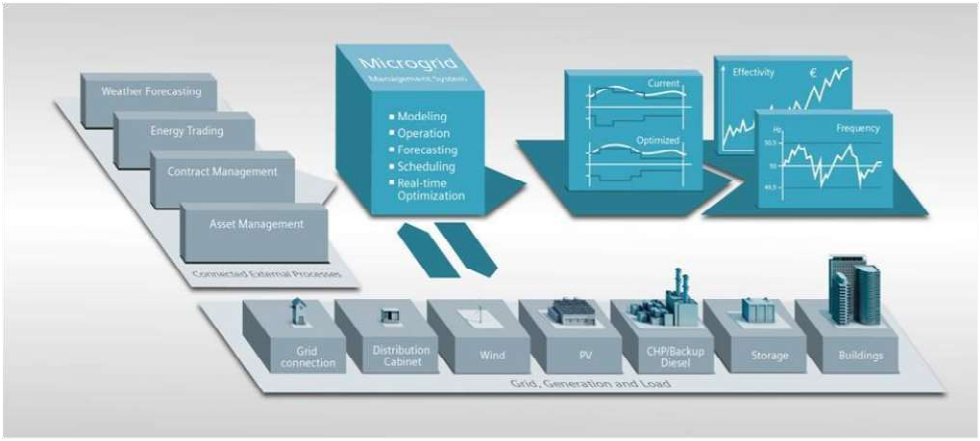

Fig. 1.2 The distribution of power source

1.2 The research actuality of multi-port DC-DC converter

With the increasing demand for renewable energy, the power generated from the battery, PV panel, and consumed by the load is needed to be controlled with converters [13].

Using too many converters not only increases the size but also makes it challenging to do synchronous for the number of controllers. With the improvement of hybrid energy generator technology, the MPCs with low cost, high power density, stable and high efficiency, were developed.

As mentioned before, there are many advantages of combining the multi-port and soft-switching [14], for example, the switching loss will be reduced with the soft-switching technique, the voltage of converter was easier to be controlled by soft switches.

1.2.1 The commonly used topologies of multiport DC converter

The topology of the MPC mainly falls into the following three types: Isolated, partly-isolated, and non-isolated converter [15][16]. The TPC was basically used in MPC application; the classical three-port DC converter topologies are shown as below.

The Fig. 1.3(a) is the traditional TPC with half-bridge topology, e.g., it combines traditional half-bridge with a bidirectional buck/boost converter, which allows the power management between the battery, input source, and load.

Fig. 1.3(b) is a TPC by adding a diode and a controllable switch on the secondary side, which controls the secondary current and regulates the output voltage. Without effective primary side switch work, this topology can control output voltage better [17], and this type of converter is called a secondary adjustment three-port converter (SATC).

The topology, as shown in Fig. 1.3(c) is another type of (SATC). The secondary side of this converter is the full-bridge circuit, which decreases the voltage stress, although the number of diodes is increased.

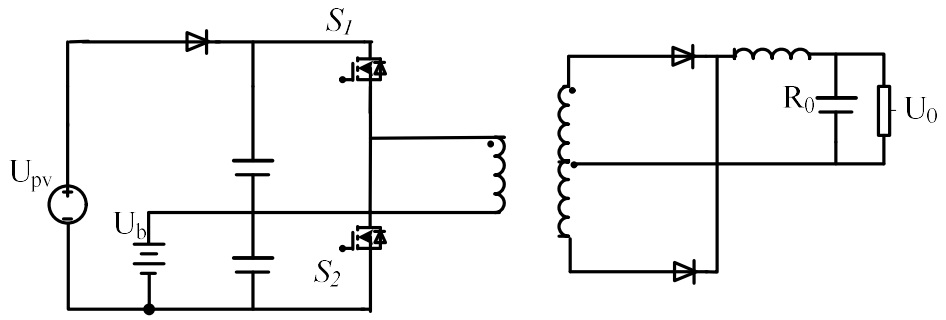

(a)

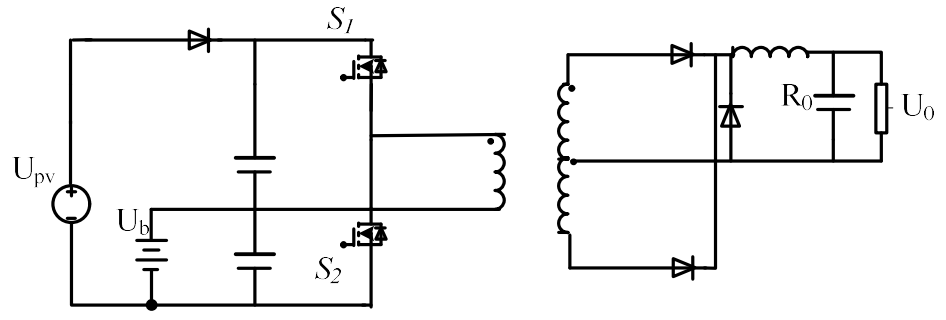

(b)

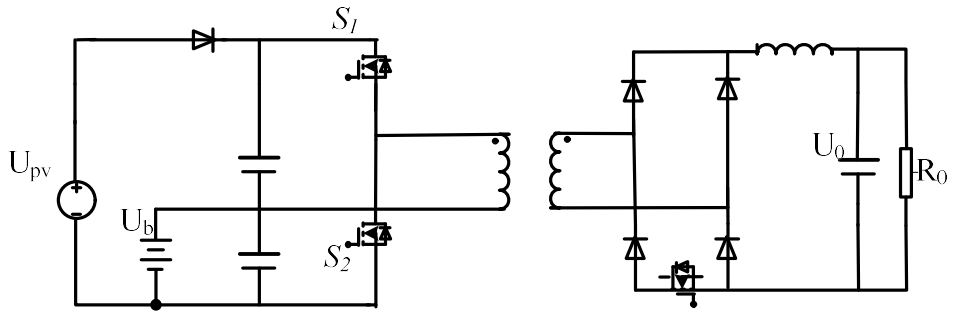

(c)

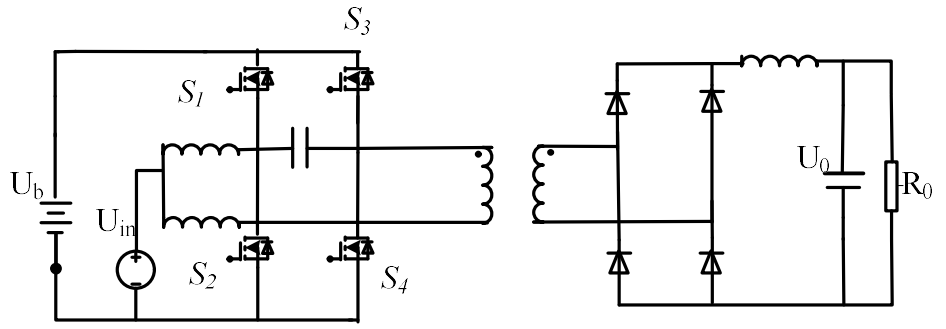

(d)

Fig. 1.3 Traditional half-bridge three-port DC converter. (a) originally …; (b) Secondary side adjustment three-port DC converter; (c) Secondary adjustment three-port DC converter (d)Buck-Boost full-bridge DC converter.

Fig. 1.3(d) draw a buck-boost full-bridge [18], the input source can be changed and controlled between U_b and U_{in} base on the bidirectional characteristic, through the full-bridge with two parallel couple of Buck/Boost converters.

These four types of TPC are able to manage the power flow of the storage battery, PV panel, and load simultaneously. However, the power conversion efficiency is low when the input voltage is low.

1.2.2 Controllers' logic of multiport DC/DC converter

The control logic of the TPC is mainly used phase-shift and PWM control, which can control and regulate voltage/current for three-port: battery charge/discharge, load voltage, and the max power point tracking (MPPT) for the PV panel. Depending on the availability of renewable energy and the state-of-the-charge (SOC) of the battery, the three-port system has different operation modes. 3shows the overall controller block diagram, with the battery current regulator (BCR), voltage regulator (VR), input voltage regulator (IVR) and output voltage regulator (OVR), the PWM shift control will be worked and control the drive signals with calculating the sampling voltages and currents by PI controller.

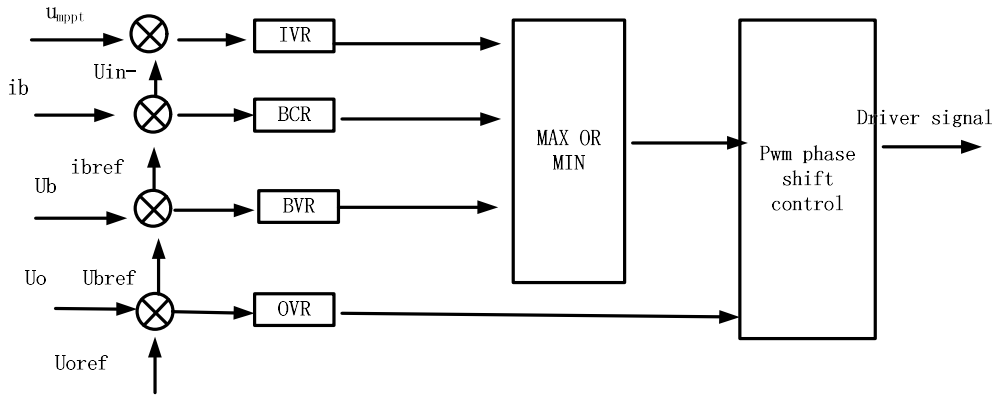

Fig. 1.4 Controller logic

Although the controller for a two-port DC converter is mature, the advanced control technique of the MPC is required.

The three-port converter paly a significant role in the renewable energy system and a lot of research work can be found. The aforementioned TPC topologies can manage power in different ports simultaneously, there are some disadvantages, e.g., the conversion efficiency is low when input port voltage is low, and it does not work for a hybrid energy system with battery. As a result, this thesis researches a new four-port bidirectional DC/DC converter.

A new type of Four-port DC-DC converter with the new GAN MOSFET is developed. It can manage the power from the PV panel, wind turbine generator, and battery efficiently at the same time. The working principle of FDC will be presented, and the small-signal model is derived from the differential equation in different operation stages. Base on the different modes change, several controllers are designed

to decouple the system, regulates the power flows of the photovoltaic (PV) and wind turbine generator (WTG), battery, and the DC-link voltage of the converter [19]. Simulation and experimental results are provided to validate the proposed controllers when the converter works in a different model. Furthermore, the FDC circuit can be applied in various areas, such as solar street lamp, fuel cell power systems [20][21] for electric vehicles, aerospace power supply systems [22], and electrical vehicle storage system [22][23].

Chapter 2：The Literature of three-port DC converter Topology

With the development of electrical engineering and information technology, the multiport DC converter was widely applying in larger areas. There are shortcomings in the hybrid renewable system, such as wind power, and solar energy will shake changing with the environment, which always becomes unstable or discontinues. In this case, a storing device, which was able to balance and manage the power flow from three-port when power short supply or excess, was required. TDC has many advantages, such as lower cost, smaller size, high reliability, higher efficiency, and higher power density. Therefore, there is great practical significance in researching multiport DC converter with these advantages here.

2.1 Full-bridge three-port DC converter

The Fig.2.1 Traditional full-bridge DC converter topology can transfer to asymmetric full-bridge DC converter topology, which combined bidirectional Buck-Boost and full-bridge DC-DC converter, constitute full-bridge three-port DC converter (FBTDC). This FBTDC can reduce the number of MOSFET switching by reusing and simplify the system's control design, especially, the power not only can be transferred between input source and storage battery, but can supply the load independently or

simultaneously as well. The FBTDC perfectly fitted for the renewable power system and a hybrid electric vehicle system.

As shown in Fig.2.2, in the asymmetric full-bridge three-port DC converter (DFBTDC) [24], switch S_1 and S_2 , S_3 and S_4 are complementary conducted. The controller of DFBTDC is able to balance three-port power flow simultaneously by changing the tow group switches' duty cycle.

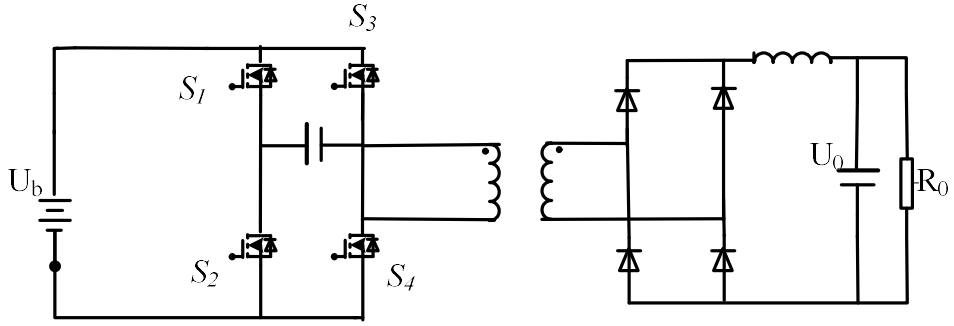

Fig. 2.1 Traditional full-bridge DC converter topology

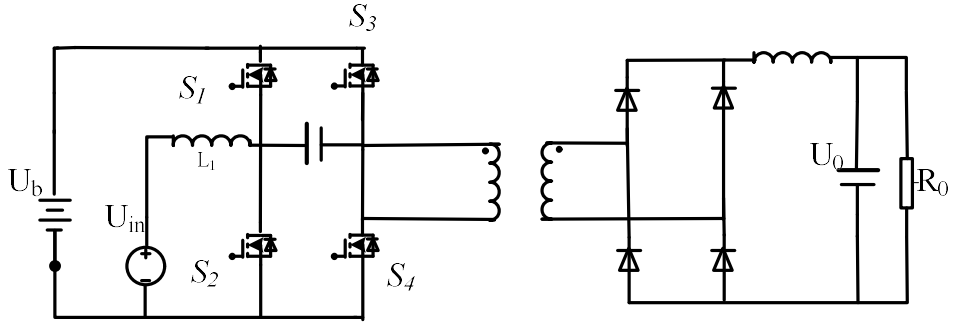

Fig. 2.2 Asymmetric full-bridge three-port DC converter

2.2 The topology of full-bridge DC converter

Here the Fig.2.3 describes a type of ZVZCS full-bridge three-port DC converter' topology. This topology is derived from Fig 2.2 topology by seperating two diodes D_3 and D_4 in the secondary side, the new topology becomes a ZVZCS FBTDC with MOSFET switch, and other components remain unchanged.

Otherwise, there are two parallel diodes D_1 and D_2 in secondary sides' upper bridge, that means, the secondary side of the converter was a full-bridge circuit, the C_0 was filter capacitor, L_0 was filter inductor, and R_0 was output load.

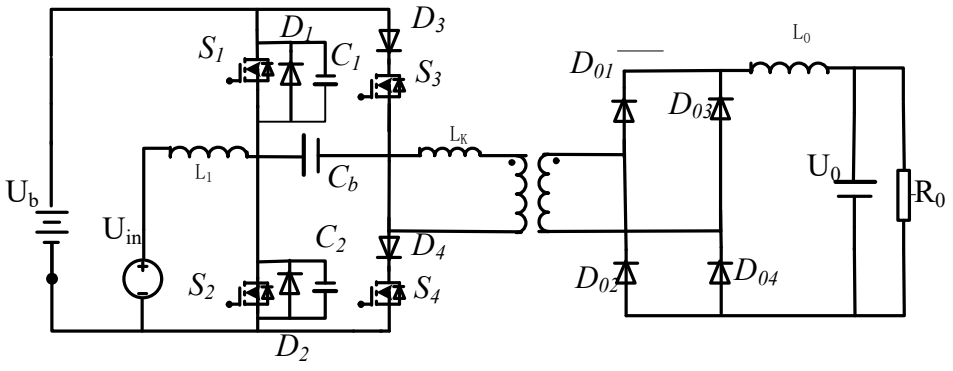

Fig. 2.3 A type of ZVZCS full-bridge Three-port DC converter's topology

2.3 The PWM controller logic of the full-bridge three-port DC converter

There are three commonly techniques used in pulse width modulation (PWM), which apply for the traditional TDC's switching complementary conduction, bipolar control method, finite unipolar control method, and phase shift control method.

The bipolar control method is the traditional approach and is commonly used in the full-bridge converter, the lead bridge and lag bridge arms diagonal power switched on and off the same time in less than half one switching period, as Fig2.4(a) shown.

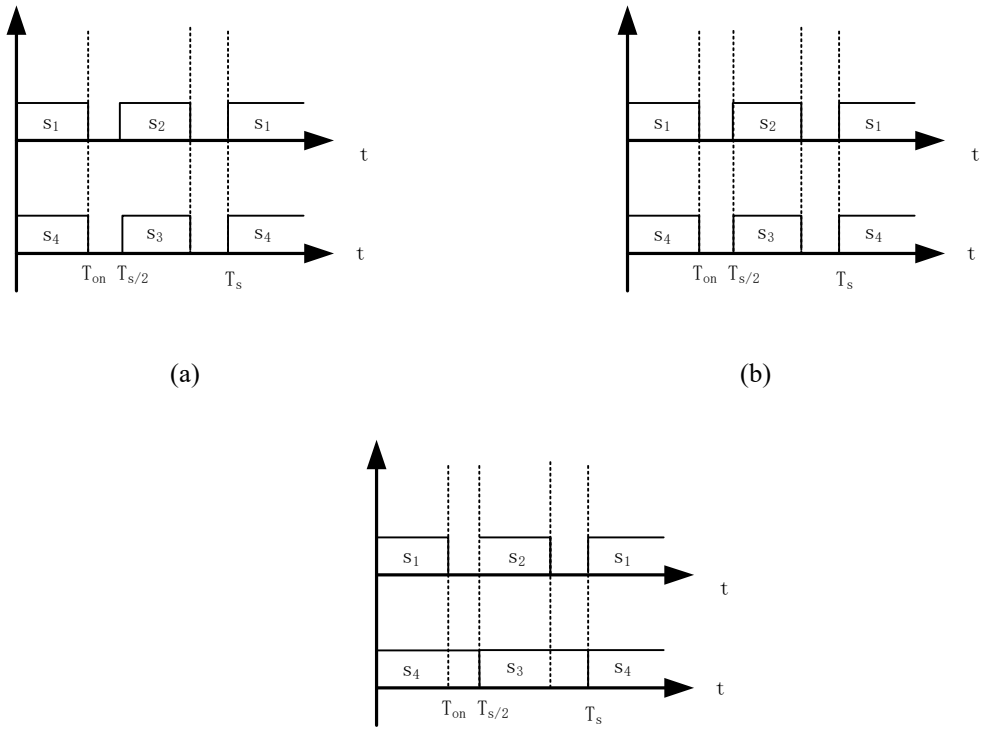

Fig. 2.4 Complementary conduction (a) Bipolar control method (b) finite unipolar control method(c) phase shift control method.

The finite unipolar control method means the power switches of the hysteresis bridge arm in the full-bridge inverter are 180-degree complementary conduction is conducted. In contrast, two power switches of the lead bridge arm are conducted with the corresponding diagonal power switches, respectively, whose opening time is less than the half switching period as shown in Fig.2.4(b) .

The final approach phase-shift controller is not only 180-degree complementary conducted of very bridge arm, but also has a phase shift plus signal before the switching period. By changing the phase shift signal, the output voltage plus width can be control, and then, the change the output voltage, Fig.2.4(c) .

Review three control techniques, whatever full-bridge circle, full-wave circle, or different control tech, the key point to operate the soft-switching control in the full-bridge inverter is to use phase shift control theory. In commonly, by using the DSP, the phase shift of full-bridge DC converter can be achieve with DSP28335 in this thesis.

2.4 The working principle of full-bridge DC converter

The ZVZCS full-bridge DC converter was used as the phase-shift tech, Fig 2.4(c) shows that there is a gap between the front bridge arm and back bridge arm [25]. S_1 and S_2, S_3, and S_4 are complementary conducted.

The converter works in three modes: signal output and input mode, double output and input mode, and double input signal output mode:

(a) Single input and output mode: when the power of input is zero, battery support load single only.

(b) Double input and single output mode: As input power lower than load power, input power, and load support load together.

(c) Single input and double output mode: When input power is more than load power, the input supplies the load and the rest of the power is stored in the battery.

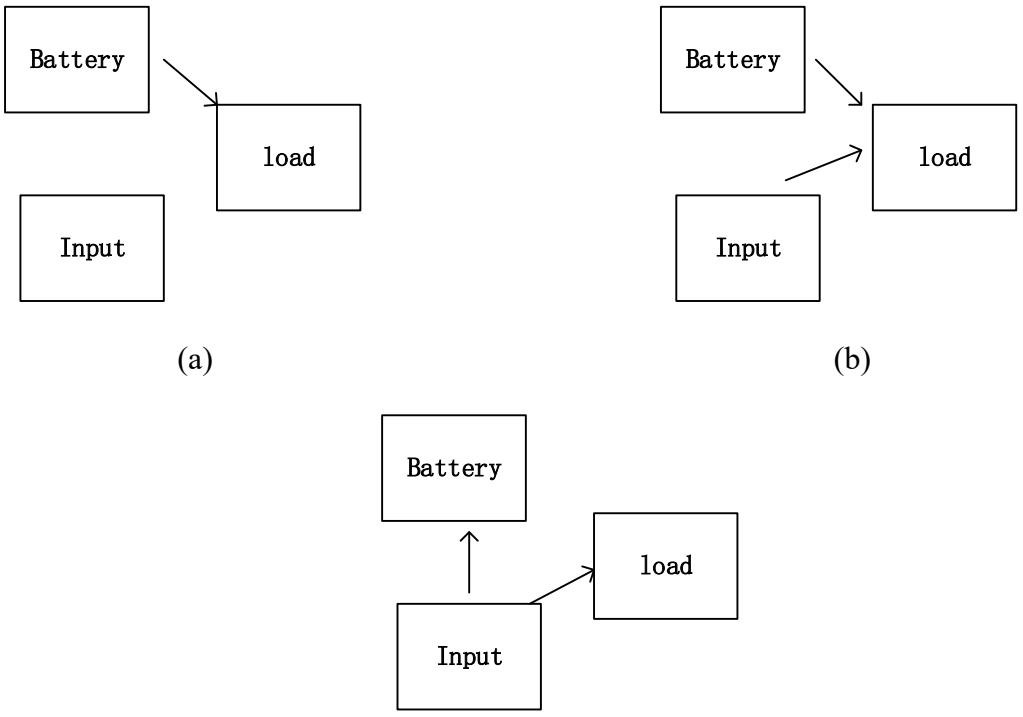

Fig. 2.5 Three port converter working mode: (a)Single input and output; (b)Double input and single-output; (c) Single input and double output.

The phase-shift controller is used in full-bridge DC converter since this full-bridge converter has eight working modes in a switching period.

2.5 The advantage and disadvantage of full-bridge DC converter

There are lots of classical topologies about three port DC converter, and depend on the main electrical isolation function between the input port and output port, the three-port DC converter can be divided into three types: Full isolated converter, partly isolated converter, and non-isolated converter.

Full isolated: There is an electrical isolation function between every port in a fully isolated three-port DC converter; the power is delivered through transformer. This topology is improved progress based on non-isolated topology.

Partly isolated: There are not only electrical isolation exits in solar port, battery port, and load port but also a common phenomenon. Compared with the non-isolated converter, this topology not only improves the safety reliability but achieves voltage match in different ports.

Non-isolated: The non-isolated converter does not have any electrical isolation function between every port since there is no transformer, it has low weight and small volume, but it has lower safety and reliability than the two aforementioned types.

The converter developed in this thesis is partly isolation bridge topology with transformer and it has isolation between the battery, power source, and load.

Chapter 3 The system design of Four-port DC/DC converter

Chapters 2 has introduced the traditional TPC and full-bridge FPC in detail. This chapter addresses the hardware design, e.g., magnetic components, for the proposed FPC.

3.1 The system structure of the Four-Port DC Converter

The overall structure of the FPC integrated with sources and load was shown in Fig.3.1 , which includes a four-port DC-DC converter, high-frequency transformers, a TI F28335 DSP, a DC-AC inverter, and three sources, i.e., a WTG, a PV panel, and battery. All algorithm is implemented in the DSP to achieve the power and voltage regulation, e.g., MPPT [26] for renewable energy sources, charging/discharging for the battery, and control the amount of output power.

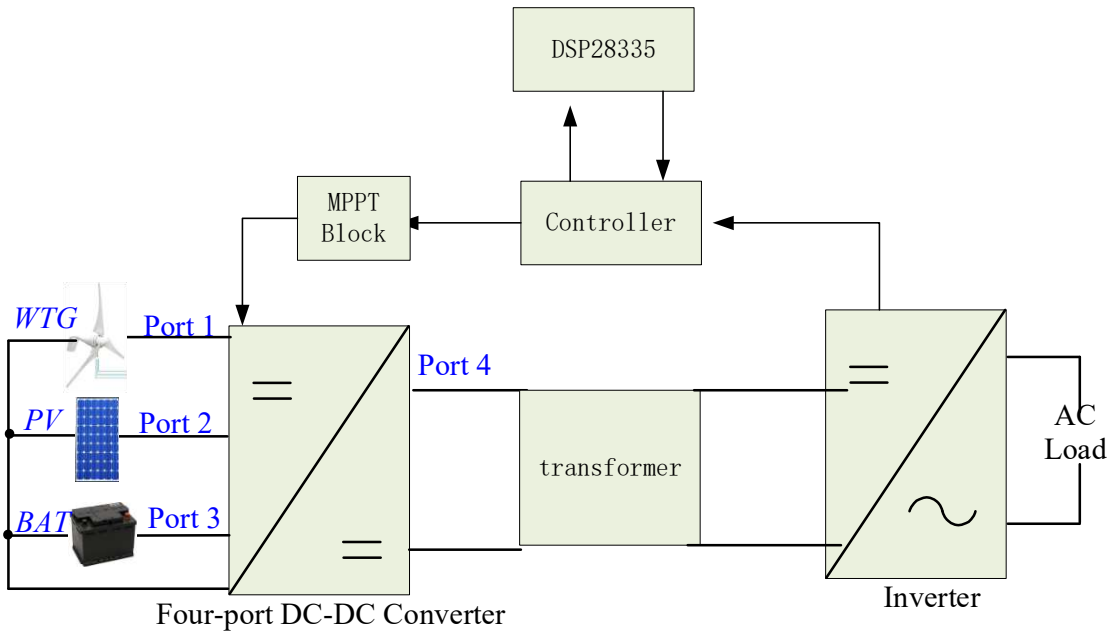

Fig. 3.1 Four-port DC converter system block

3.2 The circuit parameter design of FPC

The ideal parameters of FPC are shown in Table. 3.1, and the system components are based on these parameters analysis.

Table. 3.1 Parameters of FDC

Load battery voltage (V_b)	24V
Solar panel input voltage (V_1)	60V±20%
Wind turbine input voltage (V_2)	60V±20%
Rated output (V_{dc})	185V±10%
Switching frequency	100 kHz
Filter capacitor	

Based on these parameters, the transformers, isolating capacitor, switches, diodes, and controller will be selected or designed as followed.

3.3 The design of high-frequency transformers

The turn ratio of the transformer is designed base on the output voltage v_{dc} and the battery voltage v_b. According to Eq.(1), when $\delta=0$, the voltage gain M will be achieved the maximum value which is expected to be higher than its reference regardless the battery voltage, then the minimum valued of n can be found:

$$n_{min} = \frac{V_{dc}^*}{2v_{b,min}} \tag{1}$$

where $v_{b,min}$ is the minimum allowable voltage of the battery; V^*_{dc} is the reference voltage of V_{dc}. For any $n > n_{min}$, $V_{dc} = V^*_{dc}$ can be achieved.

To improve the effectiveness of transformers [27], a traditional transformer, as shown in Fig. 3.2 was designed; it has four windings on a core, including the primary side of turn ratio and the effect of current on the line.

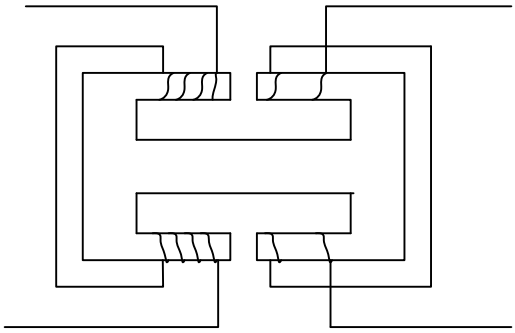

Fig. 3.2 Classical transformer structure

3.3.1 Drawing the Circuit Panel and Selection of Iron

With the development of the circuit printer, the better quality and higher current can be built in the PCB, compared with traditional transformer, the planner transformer as shown in Fig. 3.3 has the advantage of smaller volume, more winding, and better heat dissipation.

Fig. 3.3 shows the physical panel of the transformer, and there are holes in the middle to install the magnetic core. Compare the traditional transformer and panel transformer, and the panel transformer was largely reduced the size and electromagnetic interference (EMI) [28] without copper wire circle. Furthermore, the thickness of the trace is in the mile meter level, which is lower than the skin effect loss and strengths the magnetic coupling between primary and secondary sides [29]. Besides, according to the improvement of the heat dispersion performance [30] with the flat design, including PCB panel, core, and isolation layer, since the panel structure has a larger current density and smaller volume, the efficiency of the transformer will be improved obviously.

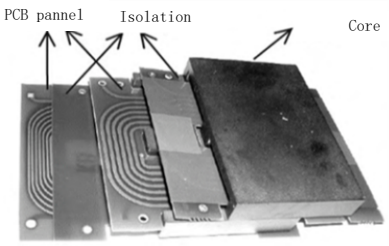

Fig. 3.3 The Panel transformer physical transformer

The PCB panel usually has a single layer panel and a double layer panel. The winding of the primary side and the secondary side was printed on the different layer but the same panel, and different layer isolation each other like Fig. 3.3. There are some advantages of a single multiple-layer panel, including smaller size and higher density. However, the higher cost and hard to work in high voltage and current stress, the single

multiple-layer PCB panel was not the first choice. Otherwise, several multiport PCB panels were a better choice for transformer, in which the primary side's winding and secondary side's winding are disturbed in different PCB panels. The several multiport PCB panels can work in high voltage and high watt situation, and lower cost, which used comment.

3.3.2 The material choice of magnetic core and device

In the processing of designing the PCB panel transformer, the soft ferrite core with a character about high permeability, lower loss, and lower cost [31], was usually used to replace traditional silicon steel core, which softs ferrite core was able to lower winding loss and core loss but increase trans effectiveness of transformers. Depend on the different design requirement, and the material was different, including MnZn, NiZn, and MgMnZn [32],[33].

MnZn ferrite can be divided into power ferrite and high magnetic ferrite, in which MnZn power ferrite has some character, including saturation flux density (B_S), initial permeability (UI), high resistivity (p) and low residual flux density (B_r). The transformer, which core made by MnZn power ferrite, can work in high temperature with lower power loss, and keep better performance in large overlay DC field. As a result, this kind of material always used in power switches, which working in a high-temperature environment.

The high magnetic MnZn ferrite material was used widely in the PCB panel transformer. Because of its high magnetic, the volume of MnZn core was very smaller

than others. This kind of core was better to fit these demands about a smaller and lighter transformer. Which mainly assemble in high demand about volumes like communication requirement and household electrical appliances.

NiZn ferrite material keeps high electrical resistivity (p), wider frequency bandwidth, low tangle loss (*tan(δ)*), lower permeability (*u*), and trans loss. Therefore, it widely used radar systems, electronic warfare, and communication filed, which demand in high-frequency response.

Finally, the MnMgZn ferrite core which is made by MgZn with little MnO has high specific resistant (*p*), low cost, and good high-frequency ability is widely used in household electrical appliances and computer filed.

3.3.3 The structure of the magnetic core

The panel PCB transformers' core usually apply RME [34], and annular structure, that E core was widely used because E core has large winding space and usable area, which can hold a bigger current, and easy to the product, lower cost.

The traditional transformer always used the AP method, but it does not fit the PCB panel transformer because the PCB panel transformer's core [35], [36] has the advantages of the smaller volume, higher power density, and higher trans effective.

Large areas can keep better heat dissipation and lower core loss but a significant size of the transformer; therefore, the design of the PCB transformer should consider the balance between temperature rising and volume.

3.3.4 Design of PCB

The design of the PCB panel [37], [38], is an important step in the processing of transformer design, which determines the transformers' working performance and property.

How to determine the spacing distance between wingding is the first challenge; it depends on the value of leakage and AC resistance. Compared with Fig. 3.4(a), as the distance increases, the leakage increased, and the AC resistance decreased [39]. Every 1mm distance longer, 9 nm leakage up and 3 mΩ down, so the winding spacing effective leakage more, the smaller leakage should be arrived by choice a proper distance. However, too small winding space will give rise to the larger voltage difference between tightly printed wire and lead to bigger distributed capacitance. Fig. 3.4(b) shows the relationship between power storage in the isolation layer and thickness that the energy stored in the insulation layer was positively correlated with the distributed capacitance. As a result, for reducing transformer loss, the insulation layer thickness should be increased and consider the balance between leakage and distributed capacitor.

Second, since the high voltage input from the transformer, lower current, but lower output voltage, higher current, so the primary side usually used series connect, secondary side used parallel connect. In high frequency, the cross-distribution method that primary side panel cross secondary side panel each was used usually to reduce the trans loss and AC resistance

From skin effect and proximity effect. Which method enhanced the coupling of windings, led to the current distributed average better.

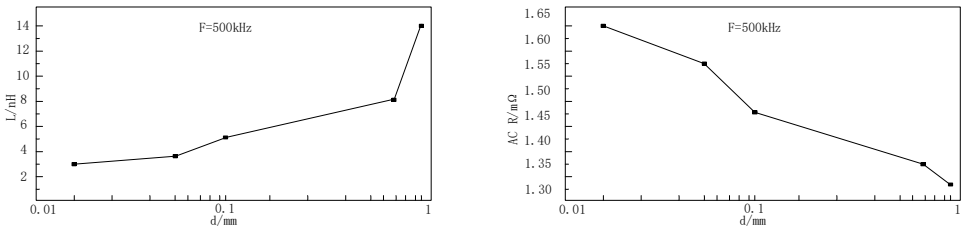

(a)

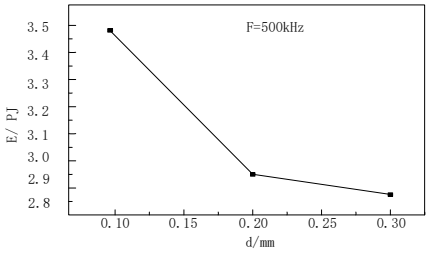

(a)

Fig. 3.4 (a) Relationship between leakage, AC resistance and spacing (b) Power in isolation layer and thickness

Fig. 3.5 shown the four classical crossing structure of a 4:1 PCB panel transformer, including (a) S-P-P-S-S-P-P-S, b) P-S-S-P-P-S-S-P cross structure, C) S-P-S-P-S-P-S-P cross structure, d) P-S-P-S-P-S-P-S cross structure.

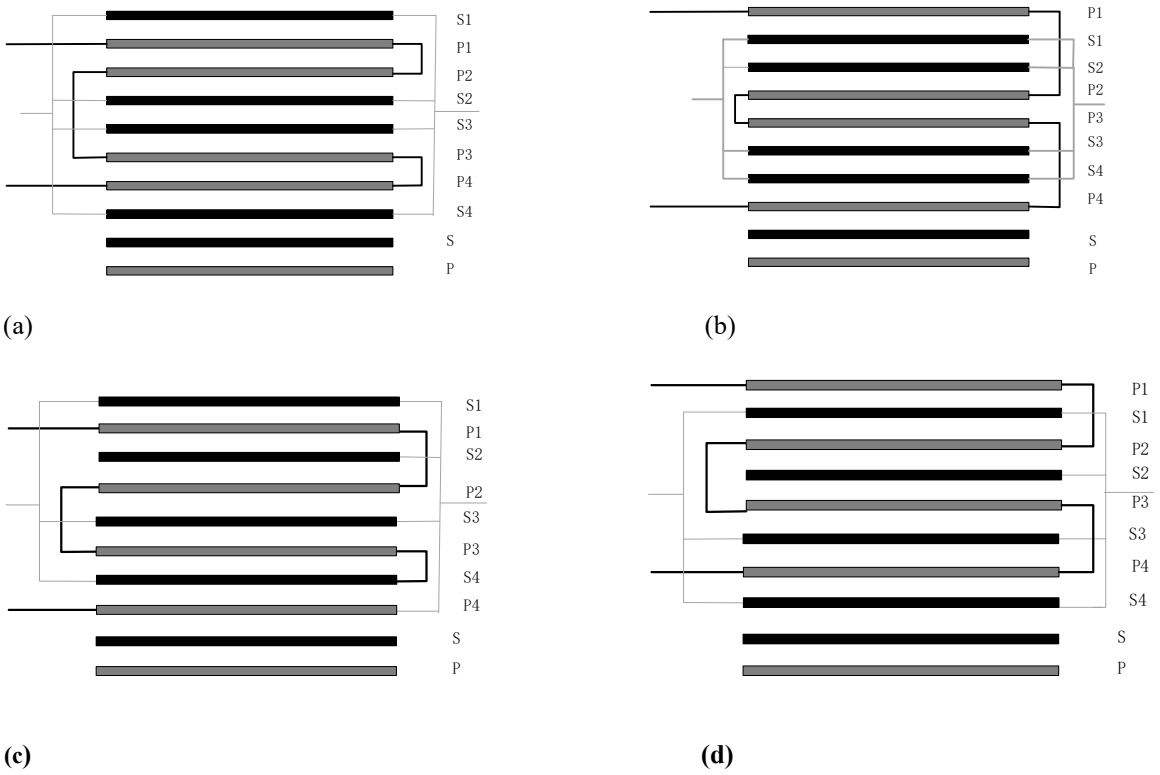

Fig. 3.5 Normally used kind of Crossing structure

(a) S-P-P-S-S-P-P-S (b) P-S-S-P-P-S-S-P (c) S-P-S-P-S-P-S-P (d) P-S-P-S-P-S-P-S

Fig. 3.6 shown the FEA tool to simulate the current density of four different crossing- structures, the current density of Fig. 3.6(a), (b) disturbed average more. And Fig.3.7 presents the AC resistance and leakage value in the different kind group, 500KHz. Obviously, models (c) and (d) keep lower AC resistance and leakage. As a

result, while frequency significant than 200KHz, the model (d) will be better; however, when lower 200KHz, the mode (d) was a better choice.

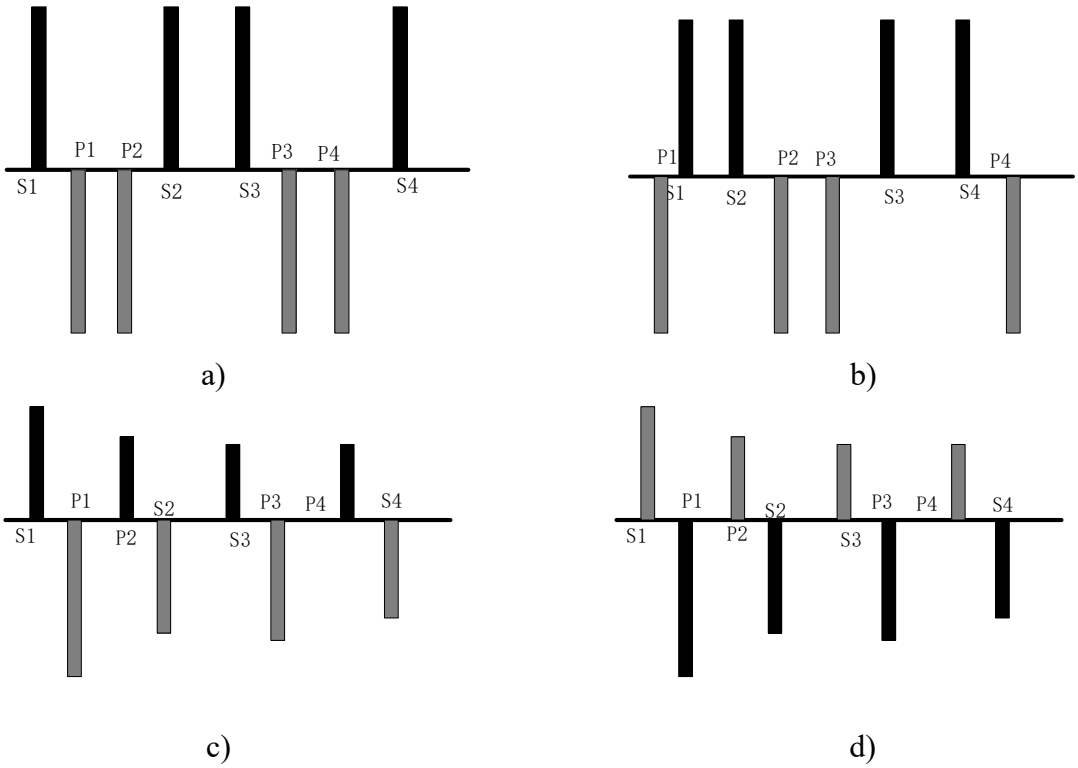

Fig. 3.6 The crossing-distribution about current density (f=500KHz)

(a) S-P-P-S-S-P-P-S (b) P-S-S-P-P-S-S-P (c) S-P-S-P-S-P-S-P (d) P-S-P-S-P-S-P-S

Otherwise, the final step was to print circuit on board, cause line by printing was too thin to hold a too large current; the material and wind of line should be including.

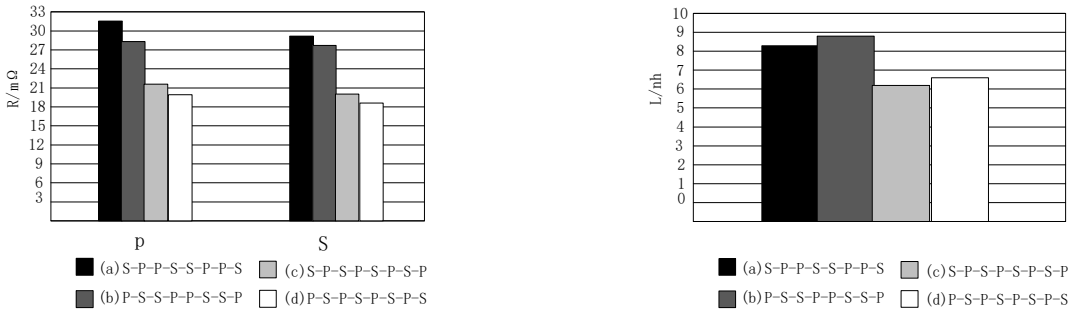

4

5 a) AC current resistance b) Leakage value (f =500KHz)

Fig. 3.7 Current and leakage value in different combination

3.3.5 The transformer production

After considering all factors, including the icon core materials, structure design, and the way of windings, the final transformer version can be decided and product Fig. 3.8.

The final transformer was a combination of two primary side windings and four secondary side windings. Respectively, the winding rate was about 1:10 (**Fig. 3.9**).

3.3.6 The leakage loss from the transformer test

According to some irresistible force effects, such as iron's heat consumption and leakage loss from windings, the power loss in the transformer was hard to avoid.

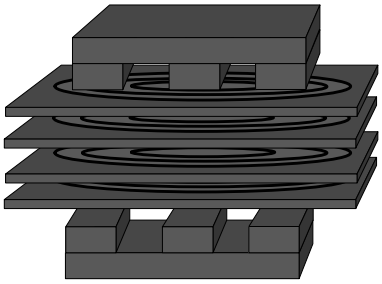

Fig. 3.8 Psychical transformer

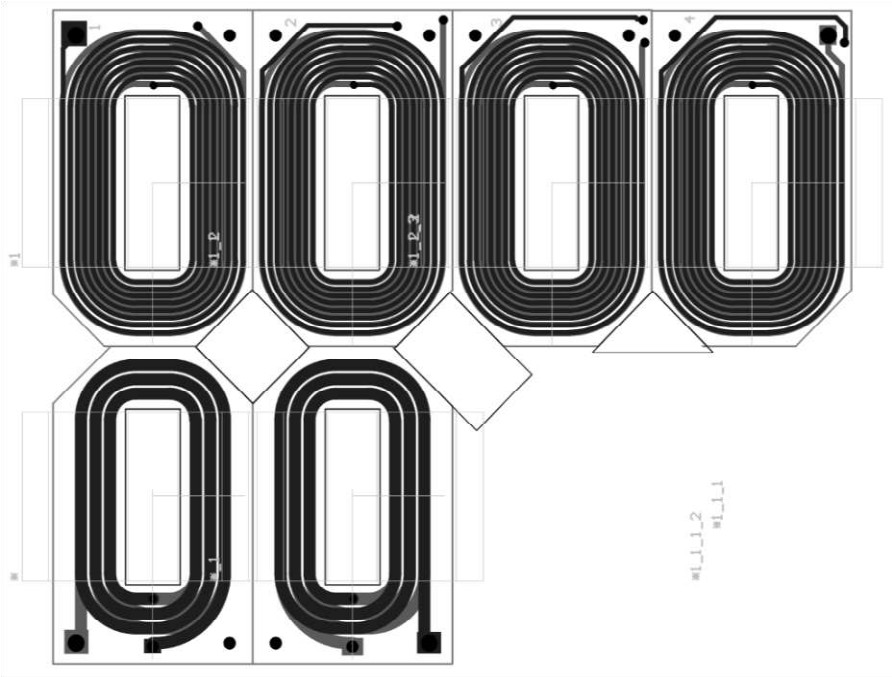

Fig. 3.9 Altium design production

Therefore, consider economy and electrical performance, the balance between power-loss and material consumption was required.

Fig. 3.10 presents the power loss from the experiment; the iron core's loss was the main current loss in transformers. On the other hand, the transformers' design about structure and winding is able to fit the requirement for power transfer. Depending on

the circuit requirement, including the current level, voltage level, and switching frequency, the best iron core can be chosen, and loss was easy to decrease.

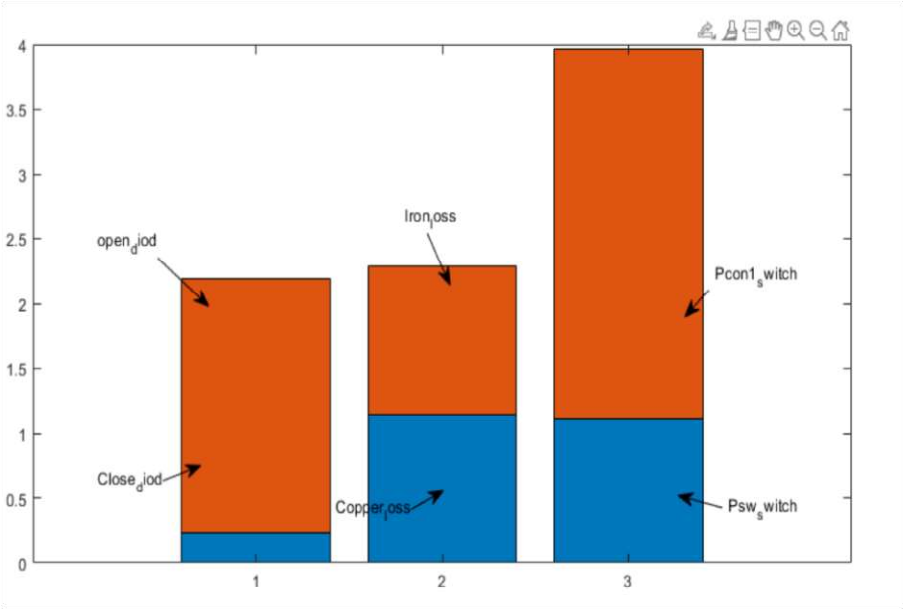

Fig. 3.10 The loss from the transformer in leakage and iron.

3.4 Switching chosen of half-bridge in converter side

For carrying the high-power change, large current push, and high-frequency switching, a reliable switch was required.

3.4.1 Introduction of the GaN material

Base on the development of semiconductor materials, various electrical electron components, respectively, semiconductor materials dominated by silicon. However, with the advent of the information age, the electron component requires much higher temperature and higher pressure material. As a result, the third-generation semiconductor materials represented by GaN have received wide attention in the world.

Its advantage can be concluded as high voltage resistance, high temperature, operation capability, high current density, high-speed switching capability, and low conduction loss.

Because of the high maximum saturation speed of GaN, it has great application potential in high frequency and high speed. Also, GaN has excellent physical and chemical stability, which allowing GaN devices to operate at very high temperatures and provide high power output. There was a higher breakdown electric field than other material, which allowed the GaN device to keep a high grid and leakage breakdown voltage and working in high voltage.

In application, the GaN device has low resistance and high withstand voltage, which contributes to a smaller volume of the circuit and higher efficiency, which largely enhances the performance of application sides, such as power source, communication, electric vehicle, and electrical field, lower the consumption, respectively.

3.4.2 The basic circuit structure of fast closed GaN device

This GaN system board, including two GaN System E-HEMTs: GS66508T(650V/30A,50mΩ) [40] or two GS66516T (650V/60A, 25mΩ) in a GaNPX top-side cooled package. The thermal pad on the device was internally connected to the source. Electrical insulation will be needed for heatsink attachment.

There was a bipolar gate drive bias with +6V and -4V for turning off is chosen for this design for a more robust gain drive and better noise immunity. The gate drive used the 5V to +10V isolated DC/DC converters, and the 10V was splinted into +6V

and -4V bias by using a 6V Zener diode. The gate drive supply input V_{DRV} was tied to V_{CC} +5V via a 0Ω jumper (FB1). Remove FB1 if separate gate driver input voltage is to be used.

Two Broadcom gate drive optocouplers (ACPL-P346) was used by half-bridge evaluation boards to drive the GaN transistors directly. The ACPL-P346 gate driver optocoupler was used to isolated and drive the GaN transistor, operating at high DC bus voltage, which loads a rail-to-rail output with a maximum output current of 2.5A to provide fast switching high voltage and driving current to turn the GaN device on and off efficiently and reliably. A diode separated the drive output, and a 10Ω gate resistor was used to limit the current for sourcing and 2Ω gate resistor for sinking.

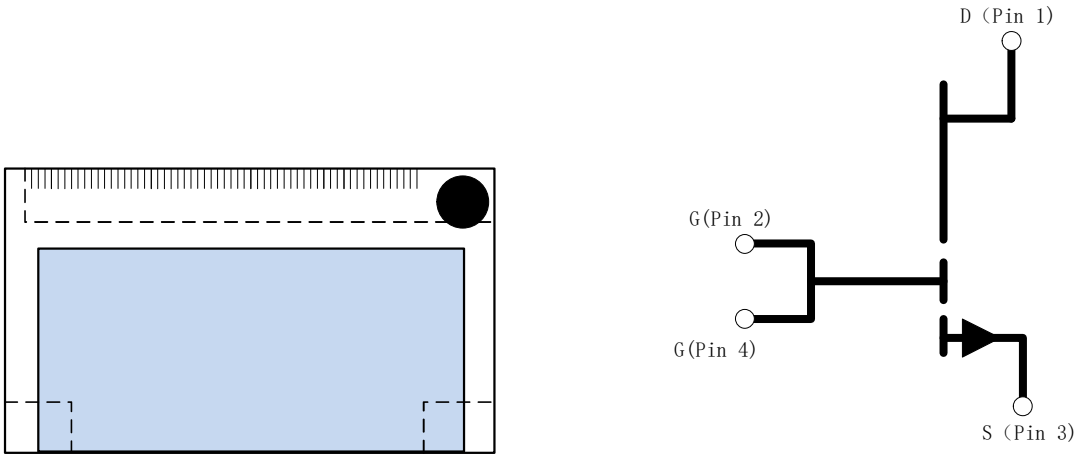

a) Package pad b) Circuit figure

Fig. 3.11 Package outline of GaN package: (a) Package pad; (b) circuit figure.

The ACPL-P346 has a propagation delay of fewer than 110 ns and the typical rise and fall times of approximately eight ns. The GaN E-HEMT switching speed and slew rate can be directly controlled by the gate resistors. By default, the turn-on gate resistors, R6/R12, are 10Ω, and turn-off gate resistors, R7/R14, are 2Ω. FB2/FB3 are

footprints for optional ferrite beads. By default, they are populated with 0Ω jumpers. If gate oscillation was observed, it is recommended to replace them with ferrite bead with Z=10-20Ω/100MHZ.

As Fig. 3.11shown followed, RS1/CS1 and RS2/CS2 are place holders to allow users to experiment with the RC snubber circuit, which is not populated. When high-frequency operation, the power dissipation for RS1/RS2 needs to be closely watched, and CS1/CS2 should be sized correctly. It's recommended to start with 33-47 pF and 10-20Ω.

The board provides an optimal current shunt position JP1 between the source of Q2 and power ground return. Which allowed drain current measurement for switching characterization experiment test like Eno/Eoff measurement.

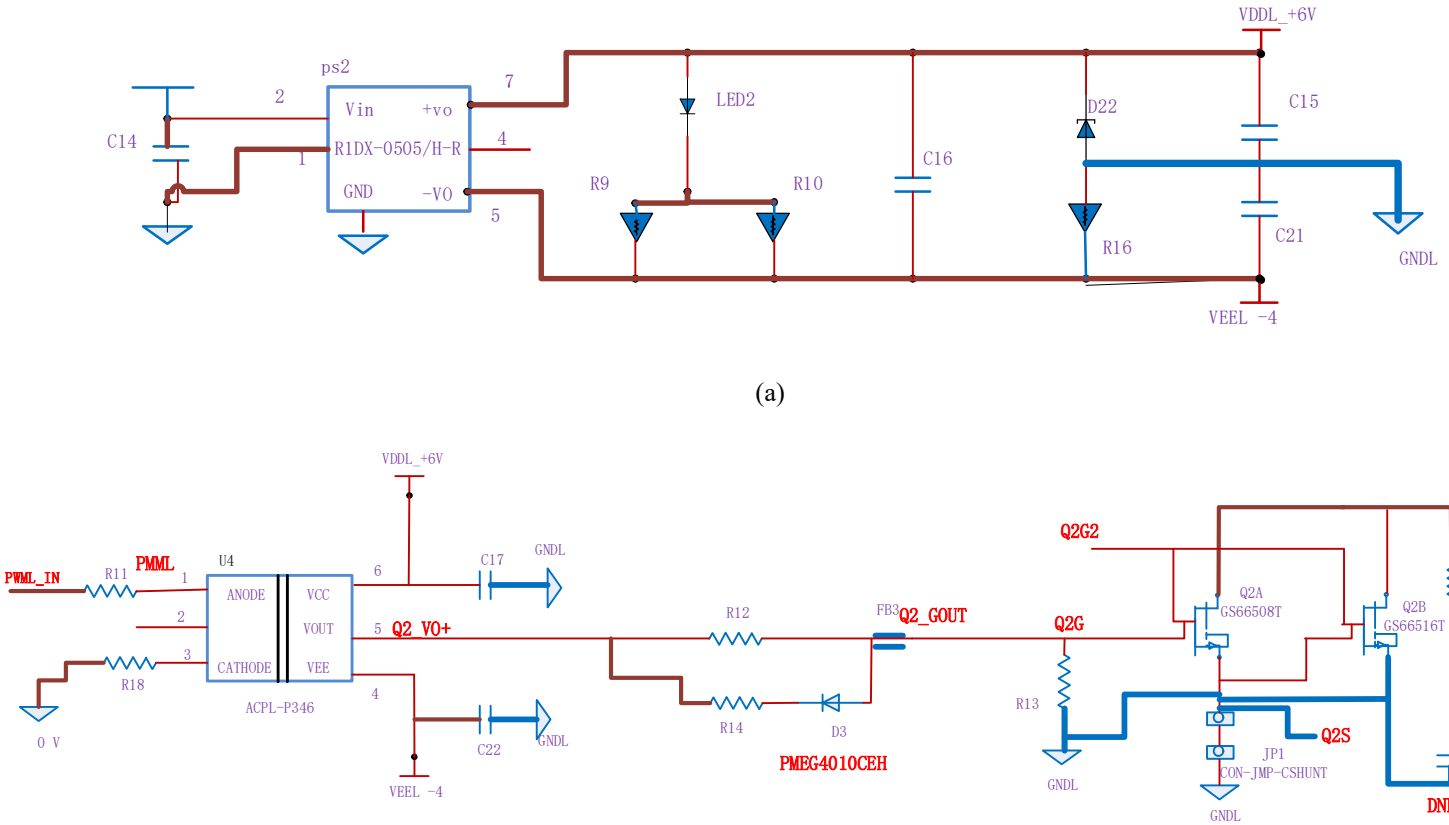

(a)

(b)

Fig. 3.12 GS66508T-Gate bias(a) and driver circuit (b)PMEG4010CEH

When measuring VSW with a current shunt, ensure all channel probe grounds and current shunt BNC output cases are all referenced to the source end of Q2 before the current shunt. By measure the current shunt, some malfunction can be quick and accurate position Fig. 3., which improves the effectiveness of the experiment. The measurement of current was inverted ad can be scaled by using: $I_d = V_{id}/R_{sense} \cdot I_d$. And the physical switching board GS6650B was shown here in Fig. 3..

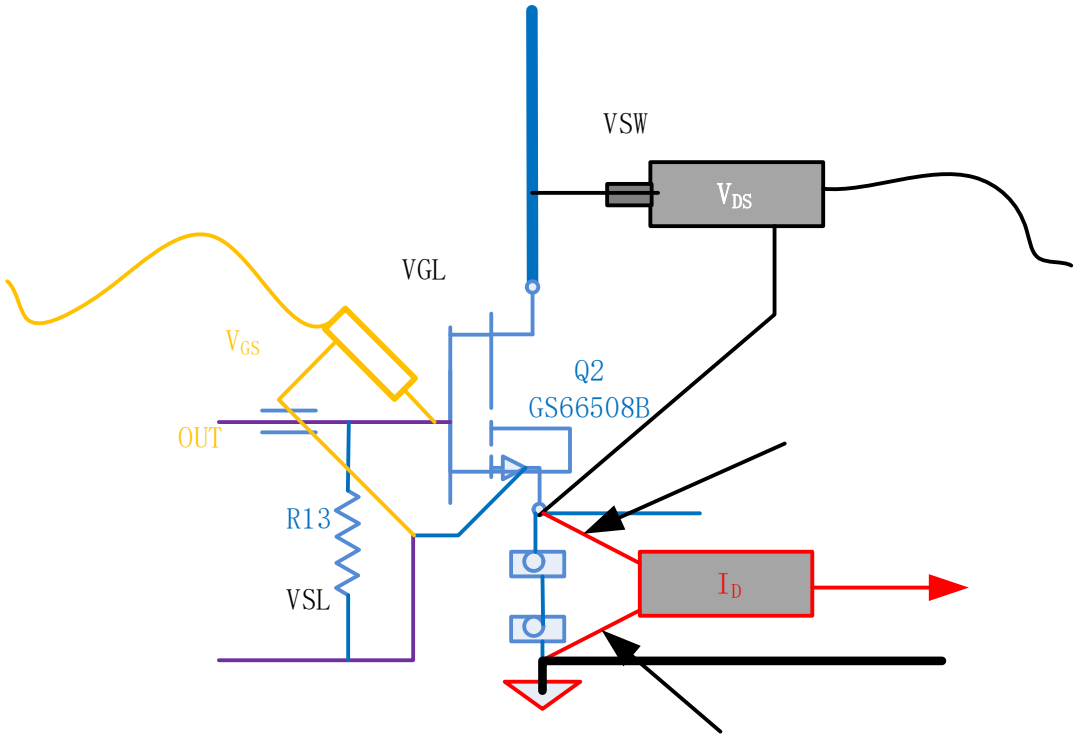

Fig. 3.13 Current shunt connection

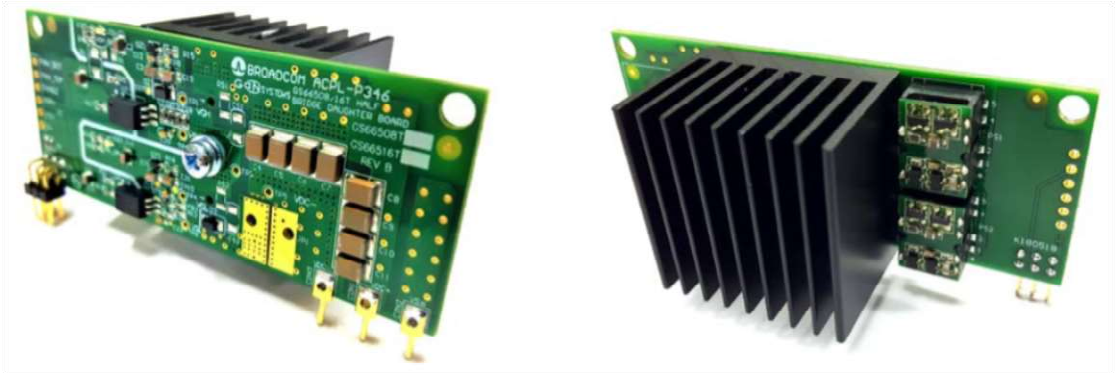

Fig. 3.14 The GS66508 GaN board assembly with heatsink attached

3.5 The PCB layout circuit and schematic processing.

Combined with the traditional full-bridge rectifier circuit and PWM phase-shift controller techique, the harmonic in converter is able to be decreased. The secondary side including four diodes, filter inductors and filter capacitor, which can wipe out some harmonic from the primary side circuit and output stable DC current, the Fig. 3.13shown followed.

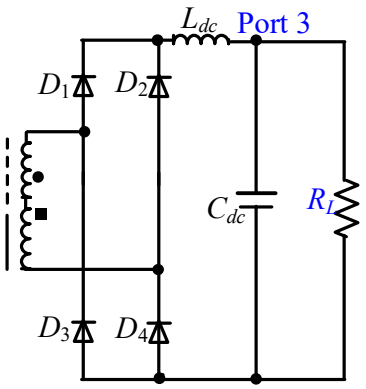

Fig. 3.13 Secondary side of DC converter

L_{dc} and C_{dc} are filter inductor and a filter capacitor on the output circuit, the capacitance was calculated as:

$$c_{dc} = \frac{\Delta i_{dc}}{4 \cdot f_s \cdot \Delta v_{dc}} \tag{12}$$

$$C_k = \frac{i_k \cdot (1 - d_k)}{f_s \cdot \Delta v_k}, k = 1,2 \tag{13}$$

where i_k and Δv_k are the average current of source k within a switching period and the desired voltage ripple of C_k.

After considering the switching, transformer, primary side, and secondary side, including the electrical parameter and power component, the basic schematic of the converter board can be drawn in Fig. 3.14, and whose PCB layout is shown in A. 2.

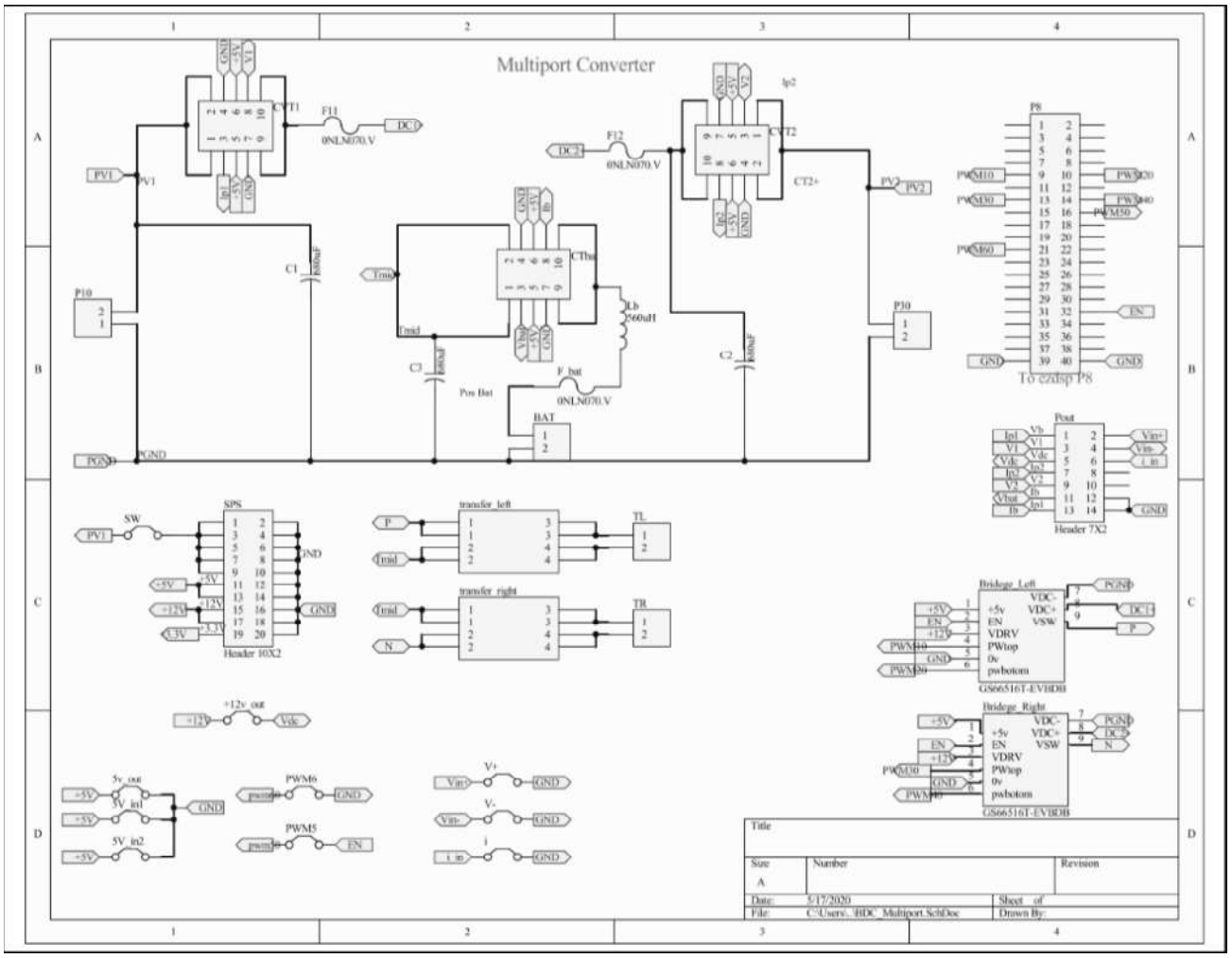

Fig. 3.14 Schematic page of converter board for reference

Chapter 4： The Working Principle of the Four-port DC/DC Converter

The research work in this thesis is to extend three-port to a four-port application without adding extra power devices. This four-port DC-DC converter inherits the advantage of traditional three-port converter highly includes integration, reliability, low cost, and small volume and improves the density and effectiveness of the transformer. The basic theory and analysis of the four-port converter will be shown as follows.

4.1 The working theory of Four-port DC converter's (FPC) topology

Fig. 4.1 showing the overall configuration of a two-stage, grid-connected four-port power integration system. The power source was connected to the FPC, as shown in Fig. 4.1 where Ports 1, 2, and Port 3 are connected to a wind turbine, solar panel, and

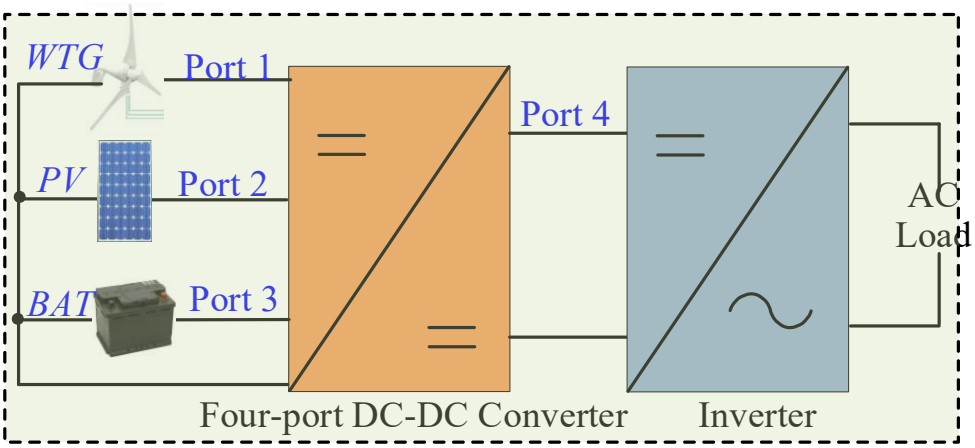

Fig. 4.1 The over viewer of the Four-port DC-DC converter

battery, respectively. The FPC's output, i.e., Port 4, is connected to a DC-AC converter for regulating the DC voltage to AC.

The FPC was derived from a phase-shift TPC [41], as shown in Fig. 4.2. The TPC has an H-bridge configuration on the primary side and a full-bridge rectifier on the secondary side. By separating the H-bridge into two half-bridge topologies that sharing the battery port, a new FPC is derived and is shown in Fig. 4.3.The FPC can be divided into a high voltage side (HVS) and a low voltage side (LVS). On the LVS, two high-frequency transformers, which turn ratio was $n = n_2/n_1$, connected to three port. On the HVS, the port 4consisting pf a full-bridge rectifier with diodes D_1~D_4 including L_{dc}, and capacitor C_{dc}.

The mainly proposed of this FPC was to regulate voltage from low voltage to high voltage required by a DC-AC inverter while achieving the following three objectives:

1) MPPT: doing MPPT for both wind turbine and solar panel;

2) Battery management: protect the battery from overcharge (discharge); the current will be limited in a certain range.

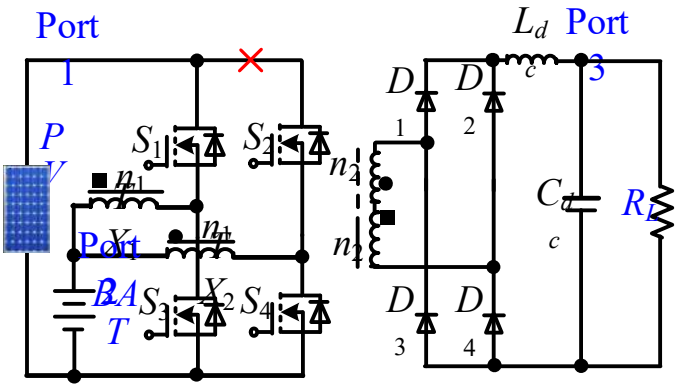

Fig. 4.2 Three-port phase-shift DC-DC converter

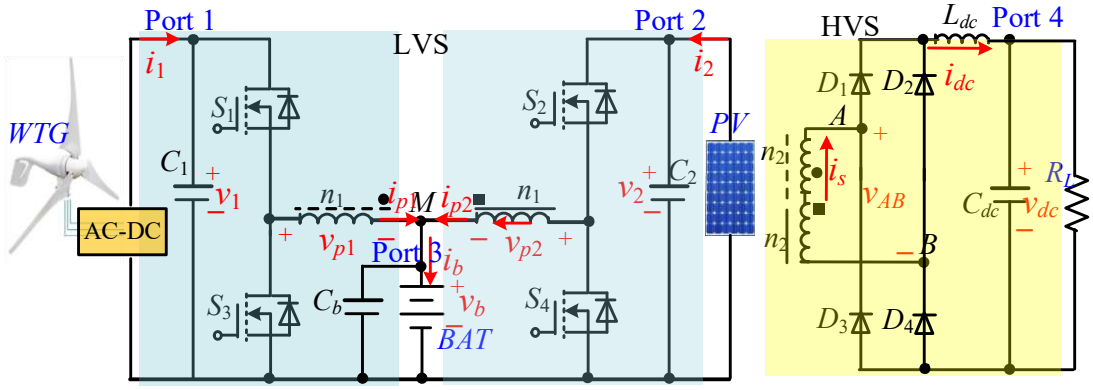

(b)

Fig. 4.3 the proposed four-port DC-DC converter

3) Bus voltage control: Regulate the DC bus voltage to a constant value, e.g., 180 V in this research. And this FDC was designed to be able to work in different operation modes regardless of the availability of wind or solar energy.

4.2 FPC operation principle and analysis

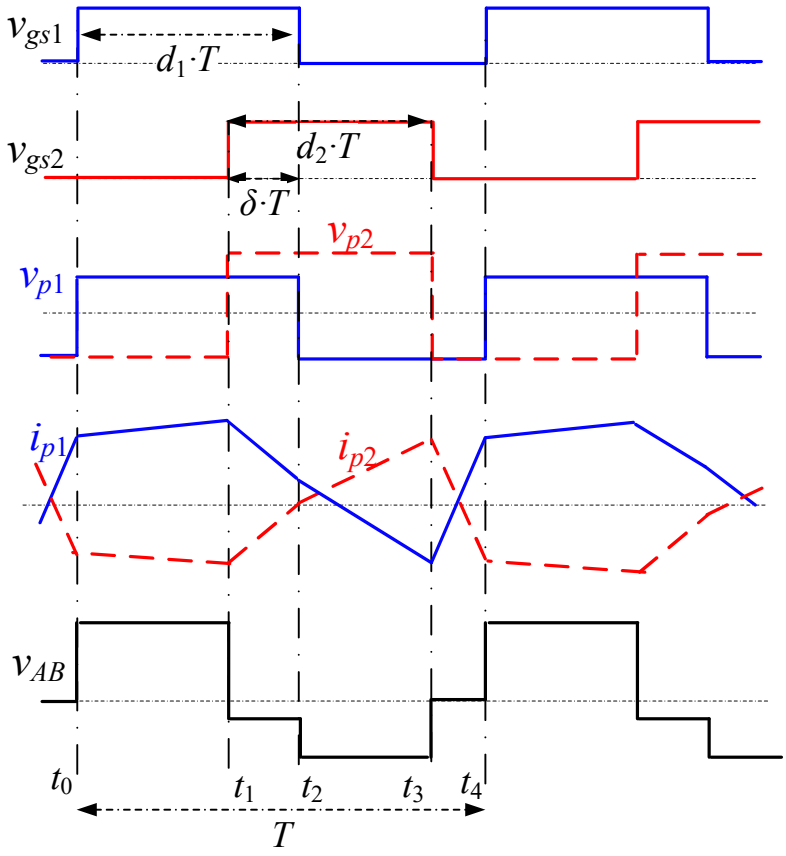

Fig. 4.4 Waveform changing with stage operation

It depends on the switching state, and the FPC can work in four different operation stages. Fig. 4.4, and Fig. 4.5 shows the and key waveforms and equivalent circuits in each stage.

Stage 1: $t \in [t_0, t_1]$ Fig. 4.4, during which s1 and S_4 are on, Port 1 (wind) support power to battery and load. Fig. 4.5(a), $v_{p1} = v_1 - v_b$, $v_{p2} = -v_b$, and the secondary voltage $v_{AB} =$

$n\cdot(v_{p1}-v_{p2})=n\cdot v_1$, $i_{s1}=i_{dc}$, $i_{p1}=i_{p2}=n\cdot i_{dc}$. The differential equation in this stage can be found as follows:

$$\begin{cases} \frac{\mathrm{d}i_b}{\mathrm{d}t}=\frac{v_1-v_T-2v_b}{L_k} \\ i_b=c_b\cdot\frac{\mathrm{d}v_b}{\mathrm{d}t}+\frac{v_b-V_{boc}}{\gamma_b} \\ n\cdot V_1-v_{\mathrm{dc}}-r_{\mathrm{dc}}\cdot i_{\mathrm{dc}}=L_{\mathrm{dc}}\cdot\frac{\mathrm{d}i_{dc}}{\mathrm{d}t} \\ i_{dc}=c_{\mathrm{dc}}\cdot\frac{\mathrm{d}v_{dc}}{\mathrm{d}_t}+\frac{v_{\mathrm{dc}}}{R_L} \end{cases} \tag{2}$$

where v_T represents the V_{DC} which is referred to the primary side of the transformer, e.g., $v_T=V_{dc}/n$; L_k is the total leakage inductance which includes the primary side and referred form the secondary side of the transformer; r_b and r_{dc} are internal resistance of the battery and inductor L_{dc}; V_{boc} is the open-circuit voltage of the battery. At the end of the stage, switch S_4 is turned off, because i_{p2} is negative, which indicates it will flow through the body diode of the switch S_2, then the switch S_2 will be turned on under the ZVS condition in stage 2 by properly setting certain dead time before S_2 is switched on.

Stage 2: $t\in[t_1, t_2]$ Fig. 4.4, during switches S_1 and S_2 are on, both Port 1 and Port 2 supply power to battery and load, as shown in Fig. 4.5(b). The voltage across the primary side's transformer are v_1-v_2 *and* v_2-v_b, then $v_{AB}=n\cdot(v_1-v_2)$. The conduction of diodes on the secondary side base on the polarity of v_{AB}, like D_1 and D_4 will conduct when $v_{AB}>0$. S_1 was turned off at the end of this stage:

$$\begin{cases} \frac{\mathrm{d}ib}{\mathrm{d}t}=\frac{v_1+v_2-v_T-2v_b}{Lk} \\ i_b=c_b\cdot\frac{\mathrm{d}v_b}{\mathrm{d}t}+\frac{v_b-V_{boc}}{\gamma_b} \\ n\cdot|v_1-v_2|-v_{\mathrm{dc}}-i_{\mathrm{dc}}\cdot\mathrm{i}\,\mathrm{d}c=L_{\mathrm{dc}}\cdot\frac{di_{\mathrm{dc}}}{\mathrm{d}t} \\ \mathrm{i}\,\mathrm{d}c=c_{\mathrm{dc}}\cdot\frac{\mathrm{d}v_{dc}}{\mathrm{d}_t}+\frac{v_{\mathrm{dc}}}{R_L} \end{cases} \tag{3}$$

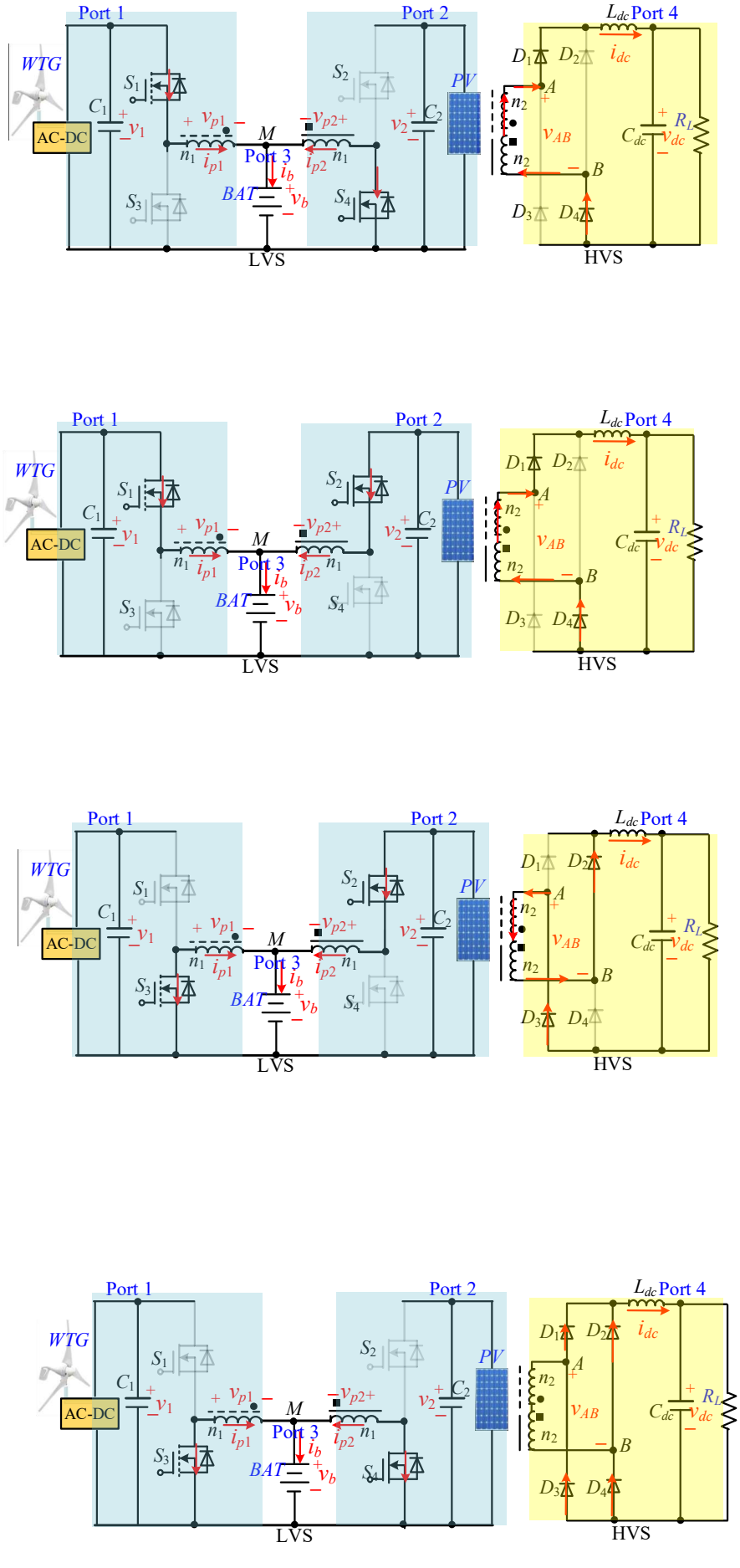

Fig. 4.5 Equivalent circuit of the different operation stage

Stage 3: $t \in [t_2, t_3]$ Fig. 4.3, during S_2 and S_4, are on, its circuit was presented in Fig. 4.5(c) and the voltage across two primary sides of the transformer are – v_b and $v_2 - v_b$. Then $v_{AB} = -n \cdot v_2$ and diodes D_2 and D_3 are on. At the end of this stage, switch S_2 was turned off, the positive i_{p2} flows through the body diode of the S_4 which then can be turned on under the ZVS condition.

$$\begin{cases} \frac{\mathrm{d}i_b}{\mathrm{d}t} = \frac{v_2 + v_{T-2} v_b}{L_k} \\ \mathrm{i}b = c_b \cdot \frac{\mathrm{d}v_b}{\mathrm{d}t} + \frac{v_b - V_{boc}}{\gamma_b} \\ n \cdot v_2 - v_{\mathrm{dC}} - r_{\mathrm{dC}} \cdot i_{dc} = L_{\mathrm{dC}} \cdot \frac{di_{dc}}{\mathrm{d}t} \\ i_{dc} = C_{\mathrm{dc}} \cdot \frac{\mathrm{d}v_{dc}}{\mathrm{d}t} + \frac{v_{\mathrm{dc}}}{R_L} \end{cases} \tag{4}$$

Stage 4: $t \in [t_3, t_4]$ Fig. 4.3, during which S_3 and S_4 are on, i_{p1} first increases with a constant slope to a positive value, $v_{p1} = v_{p2} = -v_b \cdot v_{p1}$, $V_{AB} = 0$. Due to the positive current of L_{dc}, four diodes of the rectifier are forward biased, as shown in Fig. 4.5(d). The differential equation was this stage can be expressed as:

$$\begin{cases} \frac{\mathrm{d}i_b}{\mathrm{d}t} = -\frac{2v_b}{L_k} \\ i_b = c_b \cdot \frac{\mathrm{d}v_b}{\mathrm{d}t} + \frac{v_b - V_{boc}}{\gamma_b} \\ 0 - v_{\mathrm{dC}} - \gamma_{dc} \cdot i_{\mathrm{dC}} = L_{\mathrm{dc}} \cdot \frac{\mathrm{d}i_{dc}}{dt} \\ i_{\mathrm{dC}} = C_{\mathrm{dC}} \cdot \frac{\mathrm{d}v_{dc}}{\mathrm{d}_t} + \frac{v_{\mathrm{dc}}}{R_L} \end{cases} \tag{5}$$

4.3 The steady-state analysis of FDC's topology

With the state-space average method, the average model of the converter with a switching period can be found as followed:

$$\begin{cases} \dfrac{\mathrm{d}i_b}{\mathrm{d}t} = \dfrac{v_1 \cdot d_1 + v_2 \cdot d_2 - 2v_b}{L_k} \\ i_b = c_b \cdot \dfrac{\mathrm{d}_v b}{\mathrm{d}_t} + \dfrac{v_b - V_{boc}}{r_b} \\ \dfrac{\mathrm{d}i_{dc}}{\mathrm{d}t} = \dfrac{n \cdot [v_1 \cdot d_1 + v_2 \cdot d_2 - 2v_{12m} \cdot \delta] - r_{\mathrm{d}C} \cdot i_{\mathrm{d}C} - v_{\mathrm{d}C}}{L_{dc}} \\ \dfrac{\mathrm{d}v_{dC}}{\mathrm{d}t} = \dfrac{i_{\mathrm{d}C}}{C_{\mathrm{d}C}} - \dfrac{v_{\mathrm{d}C}}{R_L \cdot C_{\mathrm{d}C}} \end{cases} \tag{6}$$

where δ is the communication duty cycle of switch S_1 and S_2,($\delta \in [0, \min\{d_1, d_2\}]$), $V_{dc} = n \cdot (V_1 \cdot d_1 + V_2 \cdot d_2 - 2 \cdot v_{12m} \cdot \delta)$.

Then the state-space model with $dx = Ax + Bu$ form (before applying small-signal) can be derived.

4.4 The Controller design of the proposed converter

The Eq.(7) shown a multiport input and output system (MIMO), which including the battery loop circuit and DC link voltage loop. Because the coupling item was not added between δ and battery voltage or current loop, like $v_b(s)/\delta(s) = i_b(s)/\delta(s) = 0$. Which d_1 and d_2 were able to control the battery voltage or current. However, the DC voltage is not only related to phase shift δ but is determined with d_1 and d_2. Therefore, an extra decoupling controller was required in the DC link voltage loop. Four controllers for managing power source were required, whose target was to regulate the voltage of DC-link to a constant value and managed the power of two power source and battery. According to the voltage second balance of two transformers, $v_1 \cdot d_1 = v_2 \cdot d_2 = v_b$, by introducing $d_1 = d_1 + d$ and $d_2 = d_2 + (V_1 / V_2) \cdot d$, and the small-signal model with $\dot{x} = A \cdot x + B \cdot u$ from can be found as follows:

$$\dot{x} = \begin{pmatrix} 0 & \frac{-2}{L_k} & 0 & 0 \\ 1 & 0 & 0 & 0 \\ \frac{}{c_b} & \frac{-1}{r_b c_b} & \frac{-r_{dc}}{L_{dc}} & \frac{-1}{L_{dc}} \\ 0 & 0 & 1 & \frac{-1}{R_L \cdot c_{dc}} \\ 0 & 0 & \frac{}{c_{dc}} & \end{pmatrix} \cdot x + \begin{bmatrix} \frac{2V_1}{L_k} & 0 \\ 0 & 0 \\ \frac{2nV_1}{L_{dc}} & \frac{-2nV_{12m}}{L_{dc}} \\ 0 & 0 \end{bmatrix} \cdot \begin{bmatrix} d \\ \delta \end{bmatrix} \quad (8)$$

where $x=[i_b, v_d, i_{dc}, v_{dc}]^T$; $u=[d,\delta]^T$. Depend on the derived model, the transfer function of battery and output voltage, such as $g_{id}(s) = i_b(s)/d(s)$, $g_{vi}(s)=v_b(s)$, $g_{vdc\text{-}d} = v_{dc}(s)/d(s)$, and $g_{vdc\text{-}\delta} = v_{dc}(s)/\delta(s)$ can be further derived.

Fig. 4.6 presents the signal flows of the overall system with four controllers $G_{cvb}(s)$, and $G_{ib}(s)$ are used for controlling v_b and i_b. And $G_{cvdc}(s)$ was to control DC current while $G_{\delta d}(s)$ was used to eliminating the influence of d from vdc. As shown in Fig. 4.6.

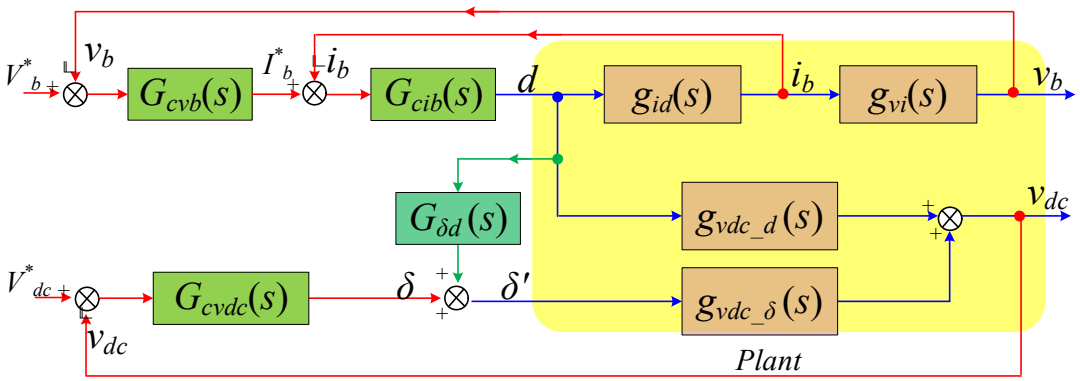

Fig. 4.6 signal flows of the controllers and plant.

The plant was a MIMO system with the coupling term $g_{vdc\_d}(s)$, which indicates the DC link voltage was not only related to d but δ. For detecting the influence of v_{dc}, the decoupling controller $G_{\delta d}(s)$ can be calculated as followed:

$$G_{\delta d}(s) = \frac{g_{vdc_d}(s)}{g_{vdc_\delta}(s)} = -{}^{V_1}/_{V_{12}m} \quad (9)$$

With the decoupling controller, the controller of the battery and the DC link voltage can then be designed separately. According to the transfer function of $g_{id}(s)$ and $g_{ive}(s)$, $Guc_{ci}(s)$ and $G_{cv}(s)$ were able to easily designed. In this thesis, $Guc_{ci}(s)$ was derived by designing the cutoff frequency around 3 kHz while maintaining phase margin more than 40 degrees, and $G_{cv}(s)$ was determined by placing its cutoff frequency less than the current loop's 1/10. And the battery current and voltage controllers can be written down here:

$$G_{cib}(S) = \frac{0.06 \cdot (s+100\ )}{s} \tag{10}$$

$$G_{cvb}(S) = \frac{0.014 \cdot (s+7\times10^4)}{s \cdot (s+3900)} \tag{11}$$

The DC link voltage was design depend on $g_{vdc\_\delta}(s)$, and its controller $G_{vdc}(s)$ was determined by suppressing the gain at 1.6 kHz less than -20 dB as well as placing the cutoff frequency at 150Hz.

$$G_{cvdc}(s) = \frac{0.3 \cdot (S+2.7\times10^4)}{s \cdot (s+3900)} \tag{12}$$

After establishing these controller designs, the next step was to organize them with an effective and accurate way of meeting power source transfer requirements, such as over-voltage or current protection for the battery. Fig. 4.6 shows the diagram of the controllers' organization. As indicated by Fig. 4.7, the battery management prevents the overvoltage and current, for example, the overcharge of $v^*_{b,max}$ and I_{bM} can be avoid. Similarly, the minimum battery voltage $v^*_{b,max}$ and -I_{bM} prevents it from over discharge. Since the renewable energy sources connected to Port1 and Port2 are

required to work properly with the battery, e.g., working in the MPPT model, four controllers are organized with two MPPT controllers in a competitive manner.

The DC-link voltage controller $G_{cvdc}(s)$ takes the voltage error and output the phase shift angle δ, the decoupling controller $G_{\delta d}(s)$ feeds d to eliminate the influence of d to δ.

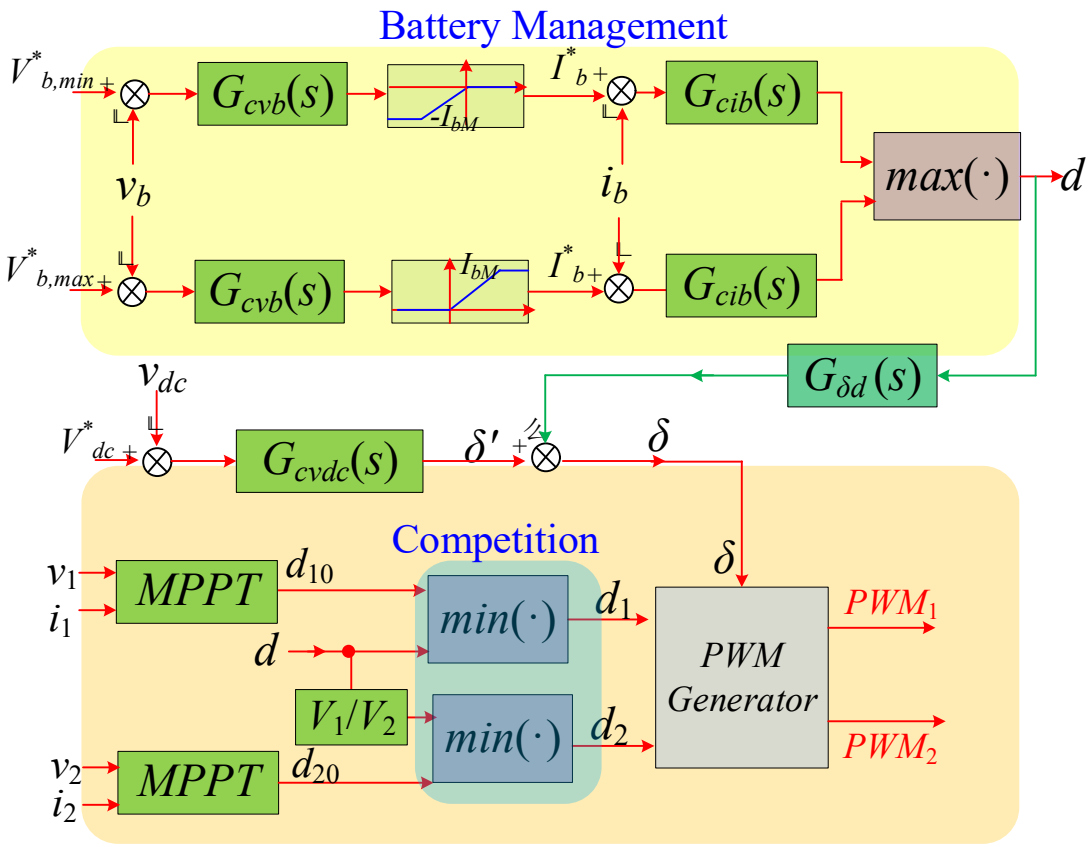

Fig. 4.7 Organization of controllers.

Chapter 5 Simulation and Experiment Verification

Within the development of technology, the computer was widely used in many areas, like electrical engineering, respectively, in a computer simulation. Which can not only to simulate really circuit and validate the principle of some ideas but also can avoid some problems that happen after an experiment on a real circuit. Before doing really experiment, design the simulation circuit on the computer and improve the design has become a common research approach, because it lowers the test number and save cost on the requirement and working time.

It's worth to mention that there is much popularity simulation software, like Saber, Multisim, Simplis, and Matlab Simulink. This thesis uses Matlab Simulink because the real-time controllers are derived from Simulink model, which accelates the implementation pace.

This chapter mainly pays attention to validate the simulation and hardware testing. According to the last chapter introduction and parameter, the simulation system can be established in Matlab Simulink and analyzed at the system level. After improving the system's controllers and logic, the prototype is built for the experiment use. Both simulation and experiment results will be provided in this chapter.

5.1 Established of the Simulation Circuit System

The simulation studies were carried out in Matlab/Simulink to verify the performance of the controller system. In our simulation, the open-circuit voltage (V_{oc}) and the short-circuit current (I_{sc}) of the PV panel were 75 V and 10A (Stander temp and

pressure) respectively, V_{mpp} = 60 V, the nominal voltage of WTG simulator and battery were 48 V and 24 V, respectively, the switching frequency was 100KHz. To estimate the performance of the controllers of the battery loops, the maximum battery charge voltage ($V^*_{b,\,max}$) and current (I_{bM}) were set to be 26.6 V and 25 A, respectively. The desired DC link voltage (V_{dc}^*) was 180 V output.

Fig. 5.1 shows the simulation detail which includes the PV1 and PV2, a couple of half-bridges, battery block, controllers, and some measurement scopes.

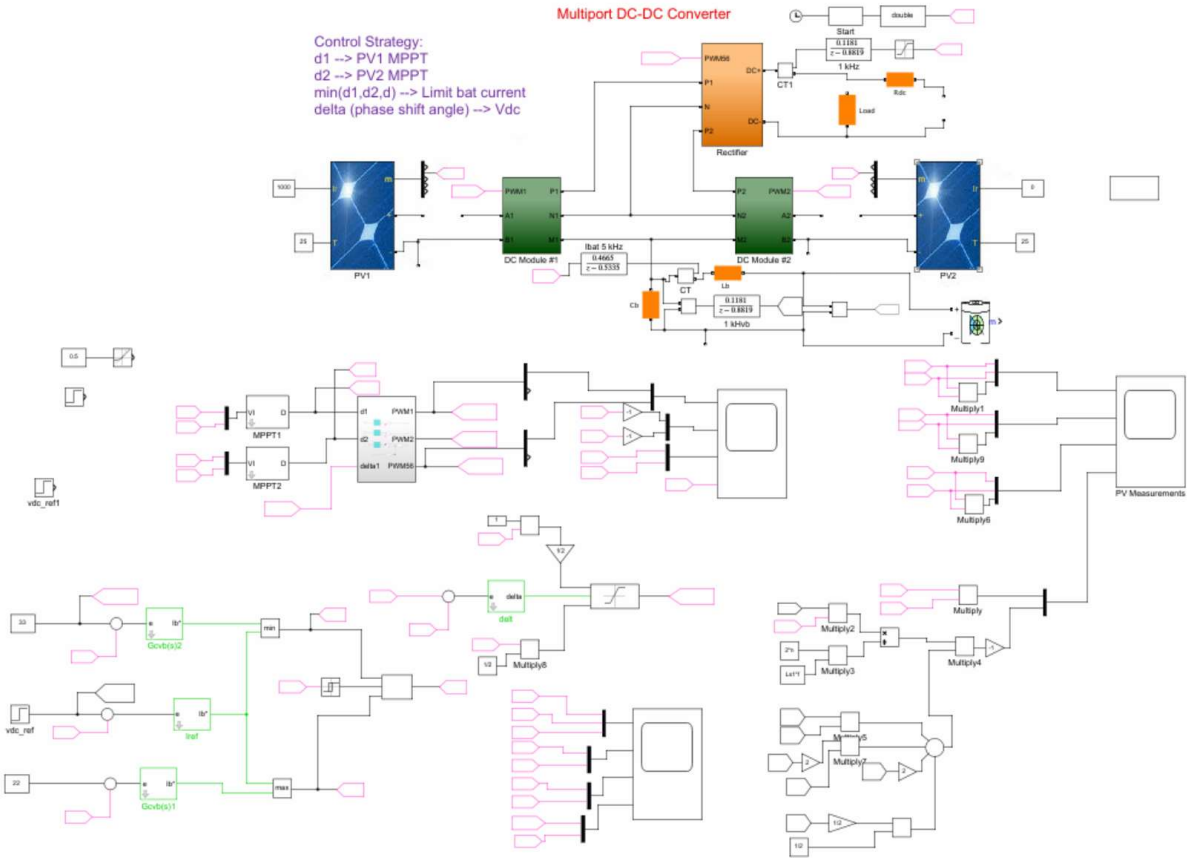

Fig. 5.1 Simple simulation graphic

According to the build-in model and function block, the input data from real-word were solved and generate various power waveforms which carried much

information about the effectiveness of these controllers were captured by scopes and shown followed.

Fig. 5.2 show the simulation result when the wind speed and solar radiation changes. As shown in Fig. 5.2, the battery voltage was below 26.6 V, which was the maximum charge voltage. The output of the $G_{cvb}(s)$ was positive and was limited to be I_{bM} (25A), the battery works in the constant current model. This mode last until t = 0.42

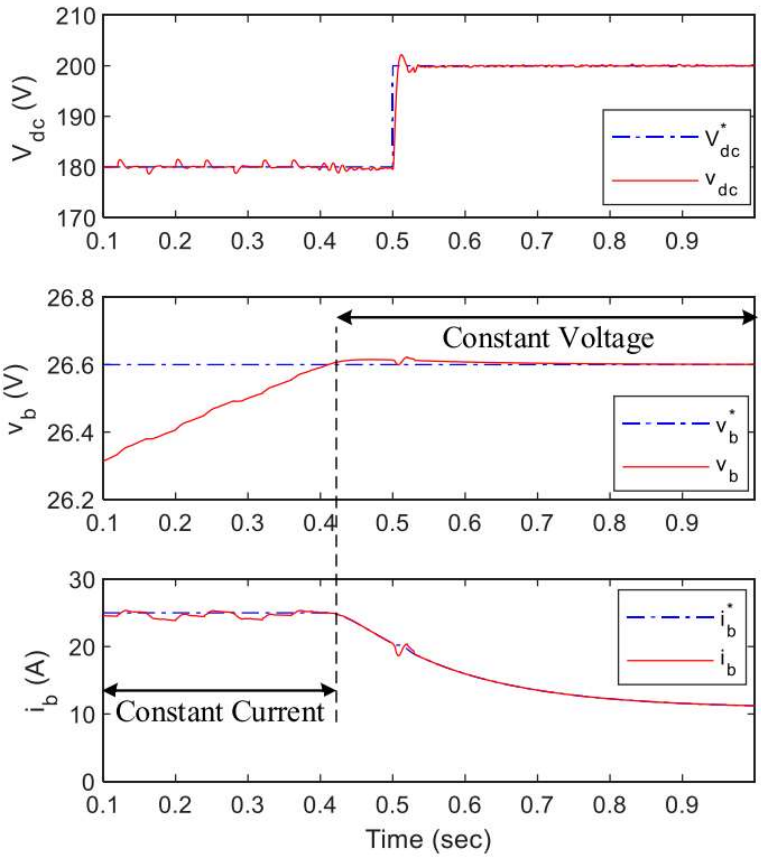

Fig. 5.2 Controller's wave graphic on simulation

sec when v_b = 26.6 V. After that, the output of $G_{cvb}(s)$ decreased from $I_{bM,}$ and the charge voltage was clamped to 26.6 V, the battery works in the constant voltage mode.

To test the DC-link voltage controller, the reference of *vdc* was changed from 180 V to 200 V while t = 0.5 sec, as shown in Fig. 5.2, v_{dc} quickly reaches to its new reference value of 200 V, which validates the effectiveness of $G_{cvdc}(S)$.

During the whole simulation period, v_{dc} does not change with the battery voltage or current unless its reference voltage was changed. In other words, the response of the battery loop does not affect the DC link voltage, which testified the effectiveness of the decoupling controller $G_{\delta d}(s)$.

For preparing the experiment setup, the key point was to make sure the correct power signal generated from DSP28335, which will be utilized to control the couple half bridges for power transfer from the primary side to the secondary side by transformers. According to coding the PWM generator, the square wave output in the scope screen, and the graphic was shown in Fig. 5.3(a). After the d changed from 0.5 to 0.6, the PWM high Fig. 5.3(b) move forward compared with PWM high in Fig. 5.3(a). Therefore, by adjusting the value of *d*, the range of phase shift could be controlled, and that was the basic operation approach of phase_shift control. After setup power signal generator, these controller blocks will be added in, and the closed-loop was completed, the system can regulate power output by phase shift controllers.

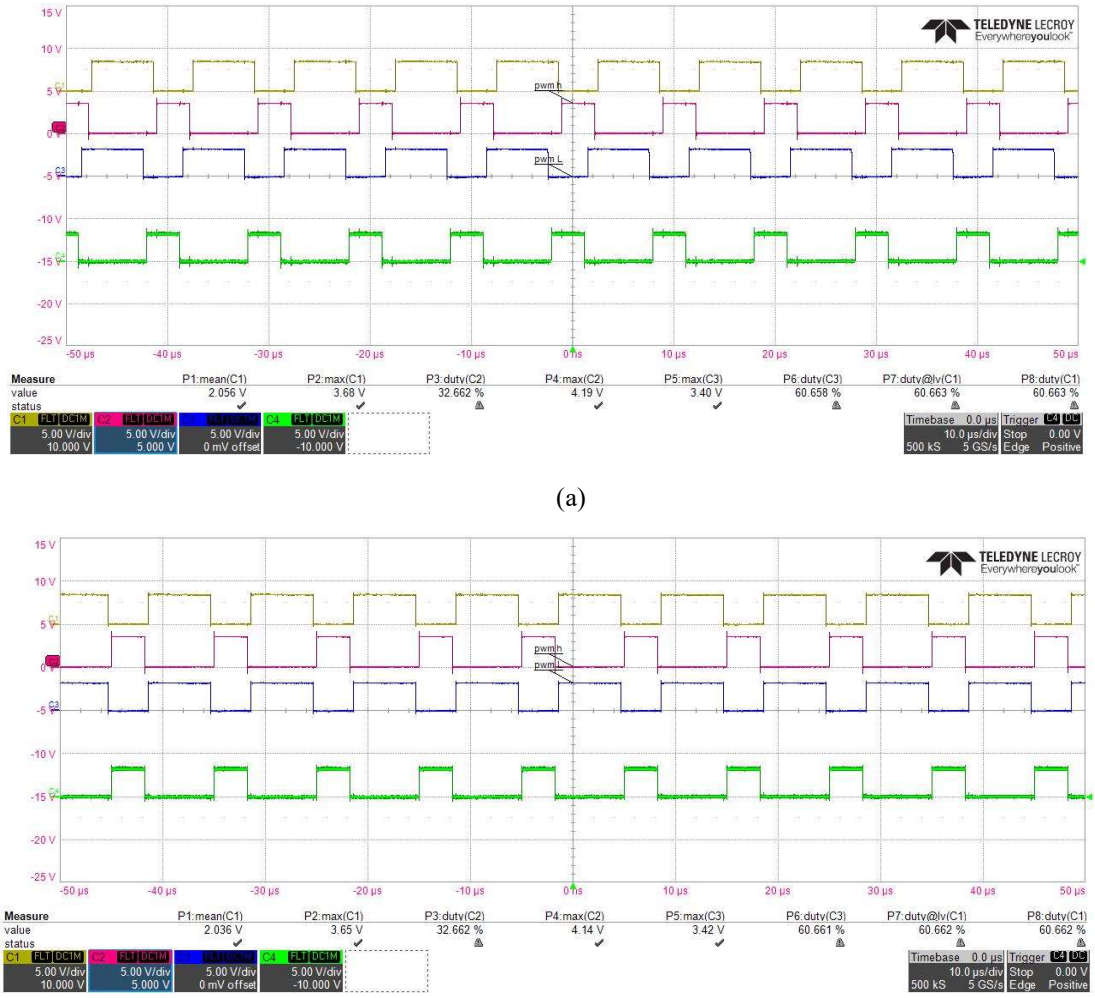

Fig. 5.3 Plus wide modulation signal while Phase shifting: (a) d = 0.5 (b) d = 0.6.

5.2 Experient result

A 1 KW prototype was built to validate the proposed four-port DC-DC converter Fig. 5.4 shown the required setup. The proposed converter was connected to a BK PVS60086MR PV panel simulator, and the WTG was generator by a couple of turbine engine which driven by DC current source. A battery bank consisting of two series-connected LCR-R1233P batteries, an eZdsp F28335 control board, and a

resistive load bank. The open-circuit voltage *voc* and the short -circuit current I_{sc} of the PV panel are 75V and 1o A, respectively, v_{mmp}= 60V. The nominal voltage and capacity of the battery bank are 24V and 33Ah. The output DC link voltage was 180V. The switching frequency f_s=100KHZ. Other parameters of the converter are shown in Table 5.1.

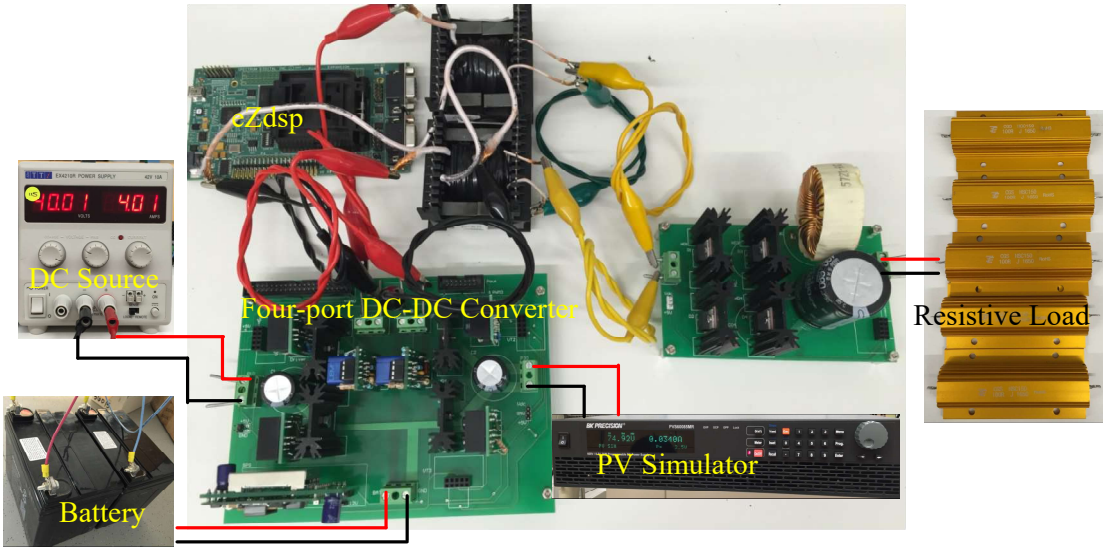

Fig. 5.4 Experiment Setup

Table. 5.1 Parameter of component

S1 ~S4	**FDPF770N15A**	**C_1, C_2**	**100 uF, 100V**
D_1~D_4	**MUR1540G**	**C_{dc}**	**330 uF, 400V**
L_k	**2 uH**	**L_{dc}**	**200 uH**
N	**45:7**		

5.2.1 The Steady-State Waveforms

presented the measured steady-state waveforms of the current primary side of the transformer, i_{p1} and i_{p2}, battery current i_b secondary side's voltage of transformer V_{AB} was exhibited in (a), $i_{p1,}$ and i_{p2} were shifted approximately 180 degrees, for example, i_{p1} was switched from positive to the negative while i_{p2} is switched from negative to positive alternately. While i_{p1} beginning increases linearly, V_{AB} has the square waveform with a magnitude of more than 180V, it will become DC after through rectifier. The positive i_b indicates the converter works in the charge mode. (b) show the measured waveform when the converter works in the discharge mode (i_b<0).

shows the gate signals (V_{gs2}， V_{gs4}) and voltages (V_{gs2}， V_{gs4}) of two switches S_2 and S_4. As shown in Fig9, before the gate signals V_{gs2} and V_{gs4} are applied, v_{ds2} and v_{ds4} have down to zero, which indicates S_2 and S_4 are turned on under the ZVS condition. Similarly, S_1 and S_3. Can be ZVS turned on as well since Port 1 and Port 2 have the same topology.

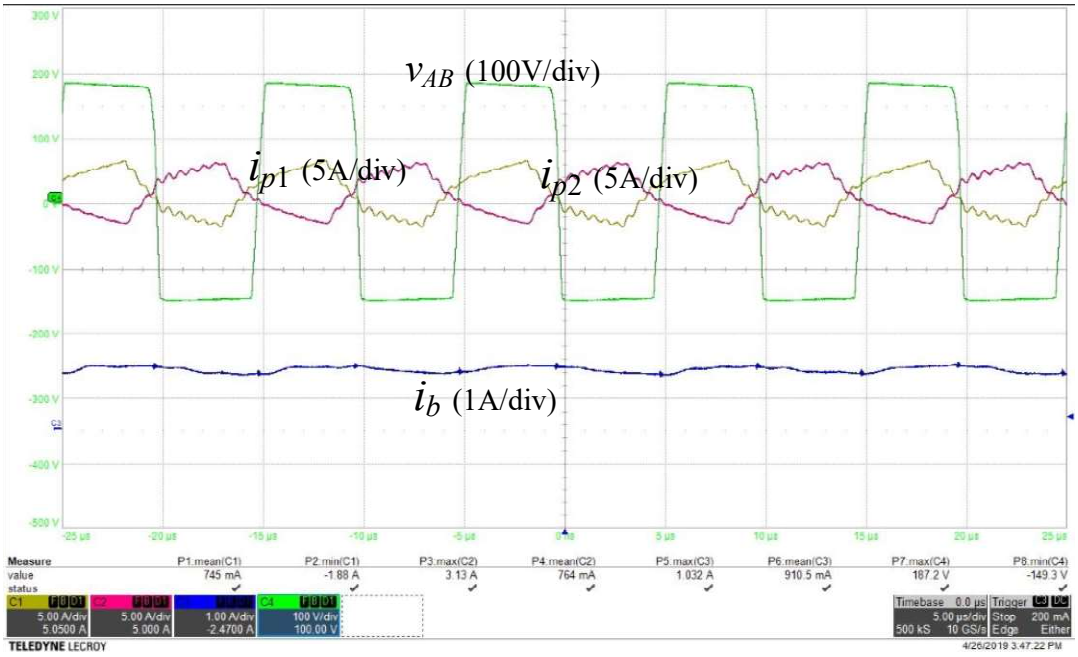

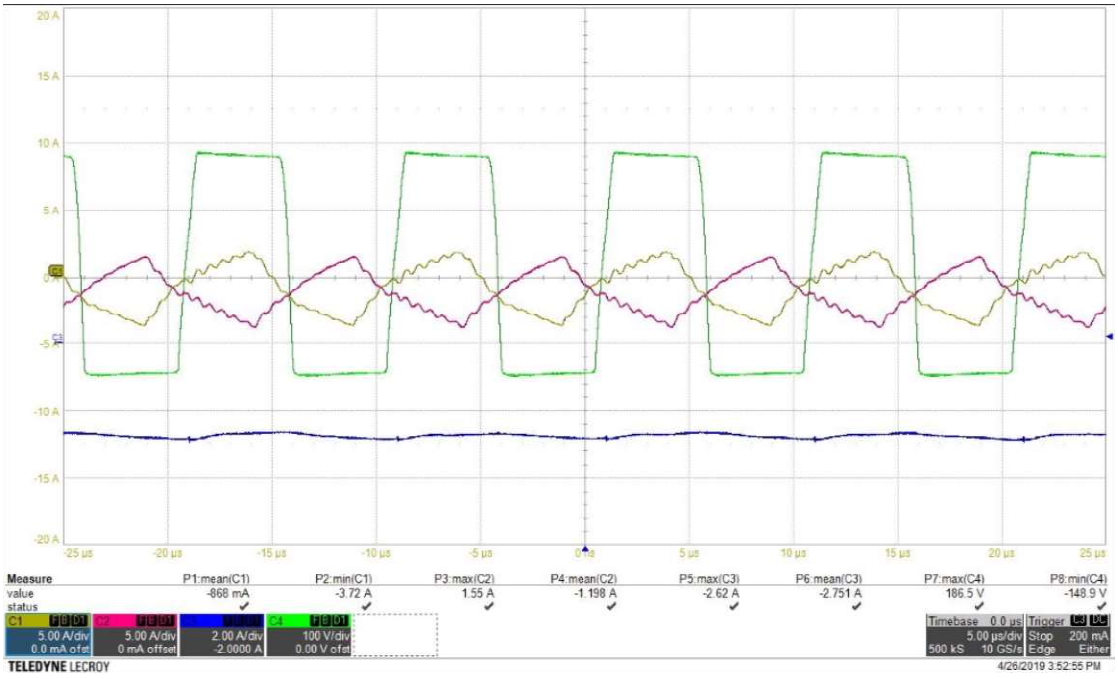

Fig. 5.5 Steady-state waveform of i_{p1}, i_{p2}, and $v_{AB.}$ (a) charge mode(b) Discharge mode

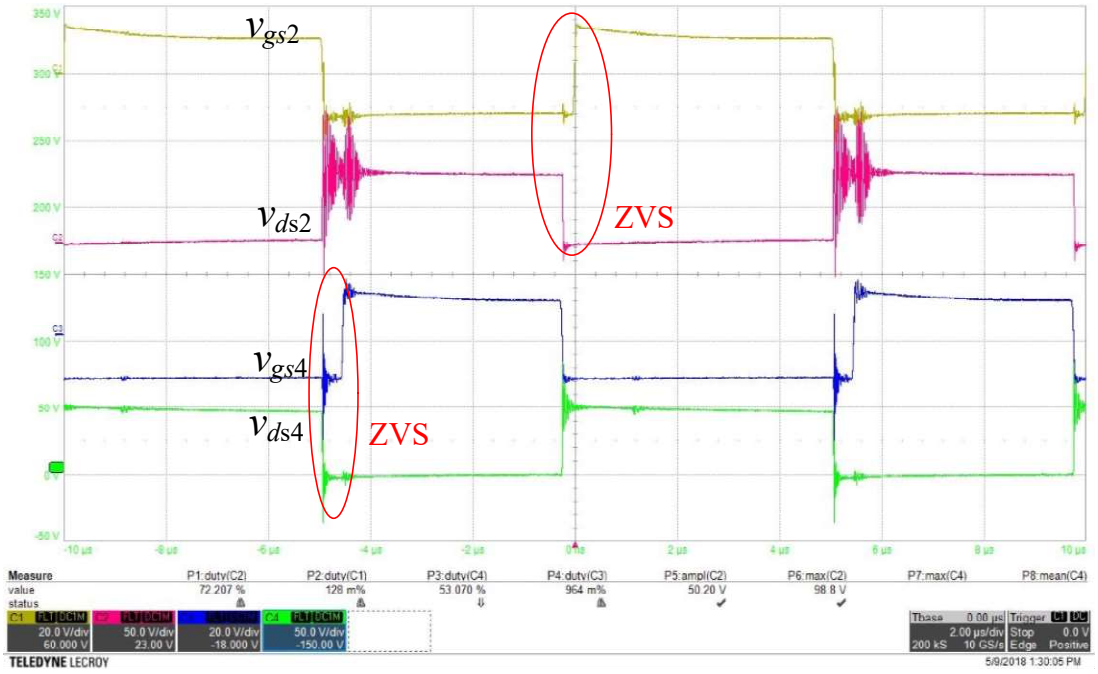

Fig. 5.6 Measured ZVS of switches S2 and S4.

5.3 Transient response

To check the effectiveness of designed controllers, the transient of i_b and v_{dc} are measured when the converter works in the different modes. Fig. 5.7 showed the simulation result when the converter was connected to one, two, or three power sources. As Fig. 5.7 shown, the converter firstly starts when only the battery was connected, the battery was linked, the battery works in discharging model, power store in the battery (P_b < 0), and *vdc* was controlled to be 180V. When t =0.5s, the wind turbine was available, the ideal maximum power point (MPP) was around 300W. It takes around 0.5 seconds to arrive MPP stage. The wind power is not enough to supply to the load, and the battery was discharged to provide the deficient power.

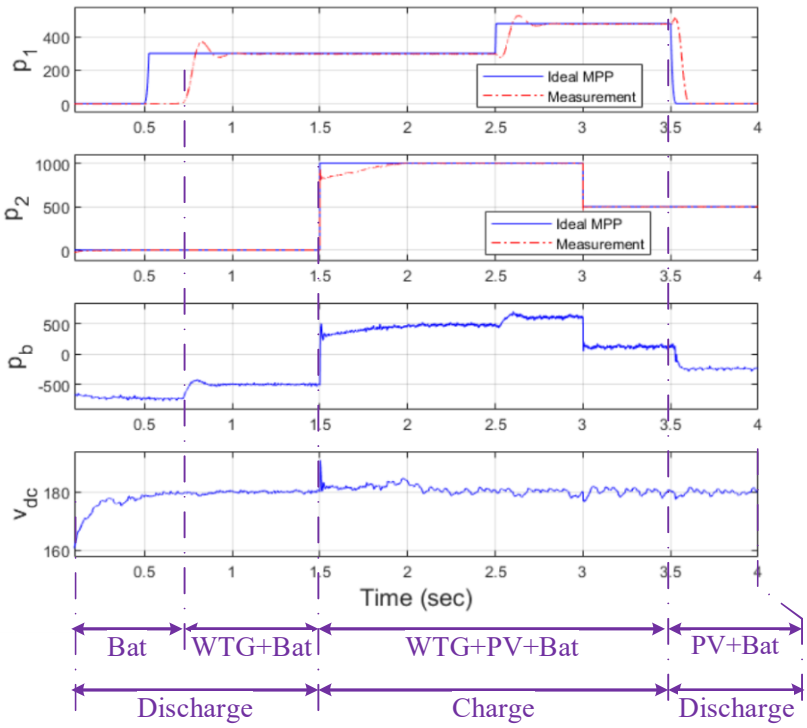

Fig. 5.7 simulation result Converter mode changing

At t = 1.5 seconds, the solar panel power was connected to the converter, which maximum power was around 1000W, both WTG and PV work at their MPPs, the battery works in the charge mode to maintain the value of v_{dc}. When the WTG was disconnected at t=3.5 second, the load was supplied by both PV panel and battery. During the various transient, the DC link voltage v_{dc} is controlled to be 180V.

Fig. 5.8 shows the dynamic process of the mode transitions. As shown in Fig. 5.8, the load voltage is maintained at 91 V during the whole process with a tiny and acceptable change. White the $t = t_1$, the wind power was disconnected, at this moment, i_1 falls to zero, i_b and i_{pv} change shortly and v_{dc} back to 91 V after a short break.

Similarly, while $t = t_2$, another power source solar panel was shuttled off, and $i_b <$ 0 at that moment, which means that the battery working in discharge mode and output voltage keep in 91 V.

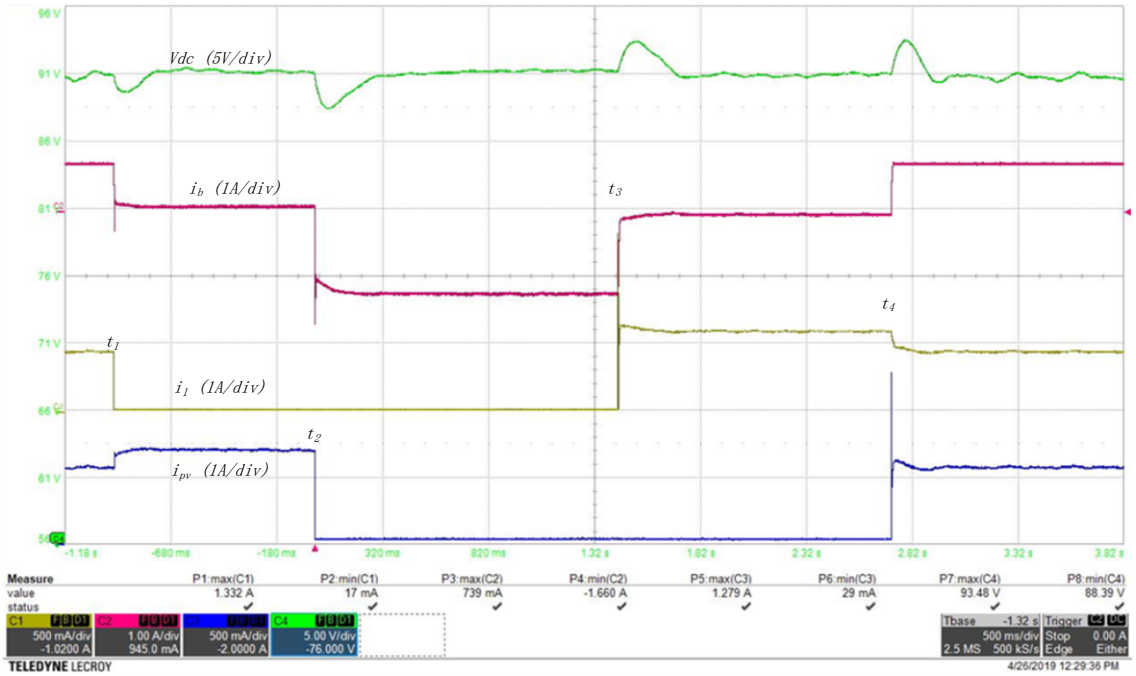

Fig. 5.8 Dynamic processing of switching while regular voltage was 91V

Then, as Fig. 5.8 shown, the wind turbine and PV panel were connected at $t = t_3$, and $t = t_4$, the i_b strongly change, and v_{dc} was regulated at 91 V.

By further optimize the experiment set up and raise the regulation voltage level to 180 V, further shown the measured waveforms of i_1, i_{pv}, i_b, v_{dc}, and p_{pv}. As shown in (a), the converter was firs connected to three sources; all currents are positive; the positive i_b indicates the battery works in charge mode. At t = -0.75 sec, the WTG was disconnected, i.e., i_1 =0, v_{dc} firstly drops to 176 V and then increases to 180 V within 200ms. The load was supplied by both the PV panel and the battery. At t = 0 sec, the PV panel was disconnected, then the load was supplied by the battery alone. During the whole transient, the battery was capable of switching between the charge and discharge mode, which validates the effectiveness of the controller of the battery. The DC-link voltage was controlled to be 180 V all the time due to the $G_{cvdc}(s)$. The maximum power of the PV simulator was set to be 47 W, as shown in (b), before and after WTG was disconnected, the PV power was around 45W, which validates the MPPT controllers.

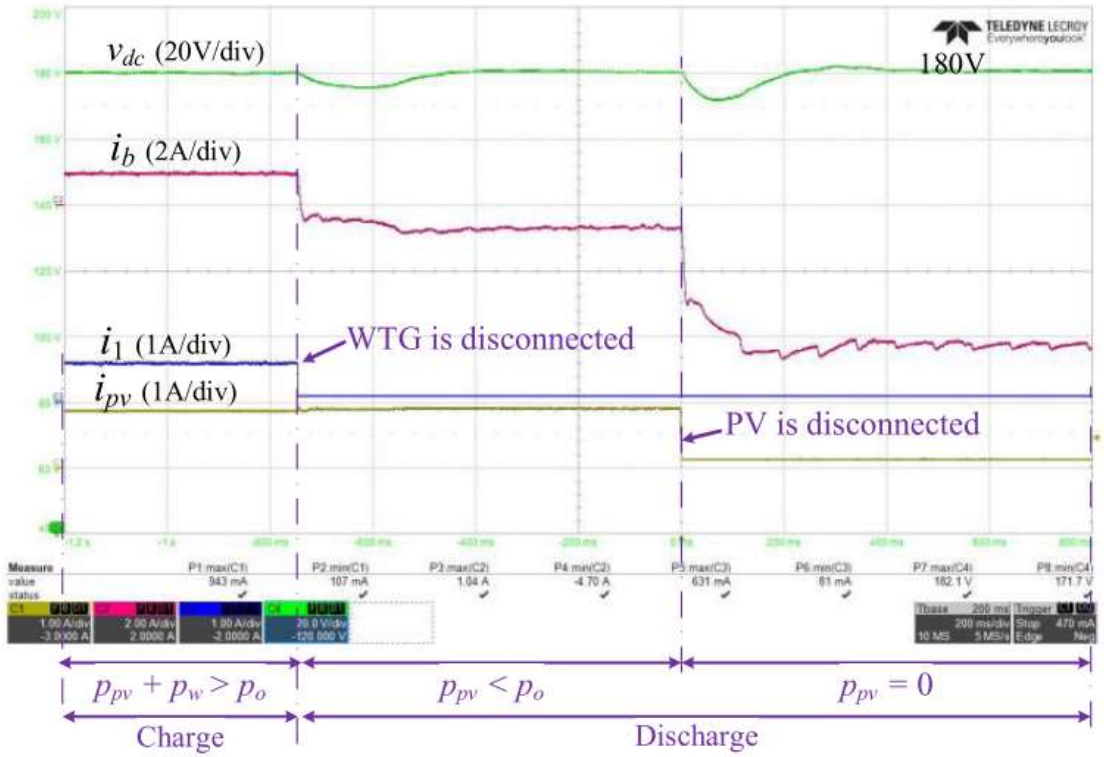

(a)

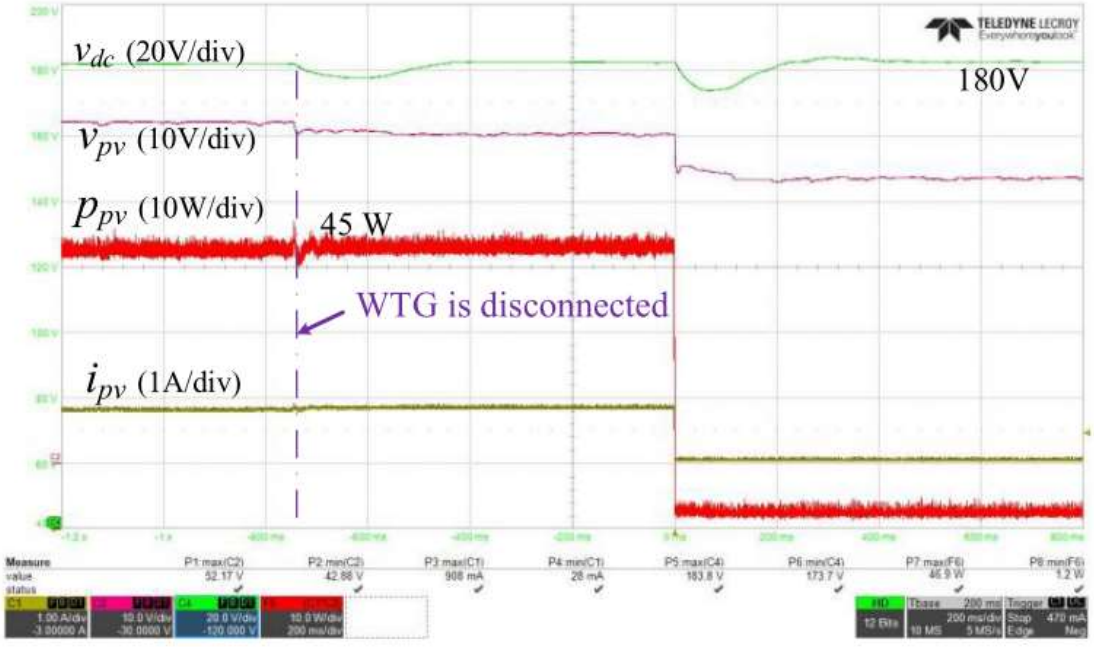

(b)

Fig. 5.9 Measured Waveforms during the mode transition in 180 V

(a)i_1, i_{pv}, i_b and v_{dc}; (b) P_{pv} and v_{dc}

5.4 The analysis of efficiency and voltage regulation

Fig. 5.10 compares the voltage curves to calculate the value from Eq. (8) with the observation from experiments when *V1* = *V2* and *d1* = *d2*. The measurement follows the calculated values, which indicates that the voltage ratio of the proposed converter was twice that of the forward converter. However, since the calculation using Eq.(8) neglects the losses of the component, such as magnetic component and semiconductor devices, the calculated voltage regulation ratio was higher than the measured value at a given duty ratio.

Fig.5.10 shows the measured efficiency while the converter work in charge and discharge modes. The charge mode efficiency was measured when the DC link related to a large resistor (500Ω) so that most powers was charged to the battery. The discharge model was tested when only the battery was connected. As shown in Fig. 5.10, the efficiency fist increases with the load, it reaches to the maximum efficiency around 50%

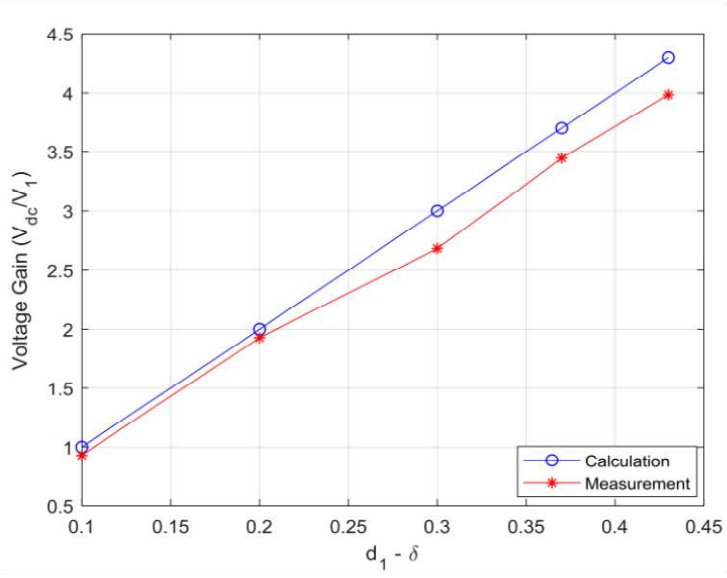

Fig. 5.10 Voltage gain vs. duty cycle

load and then decreases with the load, the overall efficiency can be maintained around 90% when the load was more than 10%。

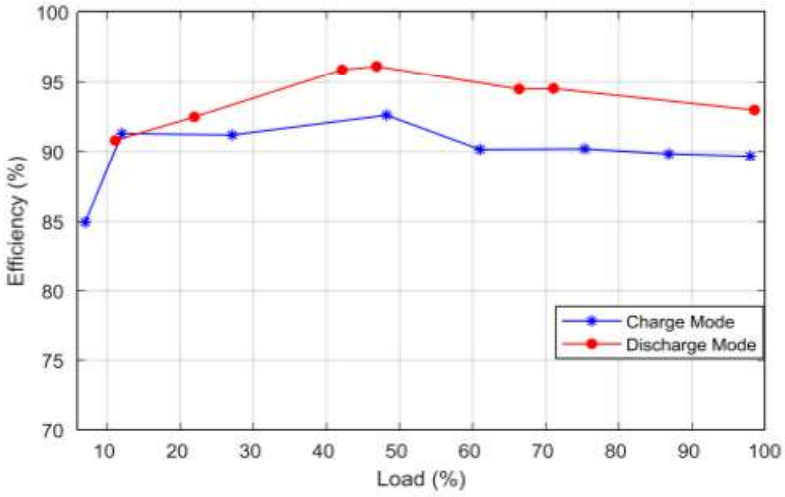

Fig. 5.11 Efficiency measure while charging mode and discharge mode

Fig. 5.12 shows the power loss distribution in both charge and discharge mode at 50% load, which in the vicinity of their peak efficiencies. In both modes, the loss of four switches cost about 50% power. As shown in Fig. 5.12(a), in the charge mode, the losses of the four MOSFETS(Couple half bridges) constitute 49%of the total loss of the converter; the diodes in the rectifier and transformers constitute 20% and 31%, respectively. Similarly, the loss in the discharge mode as shown in Fig. 5.12(b), 25% and 27% loss are distributed in diodes and transformers.

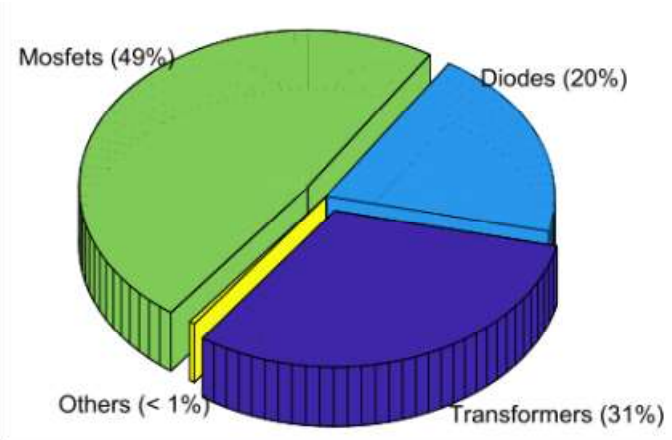

(a)

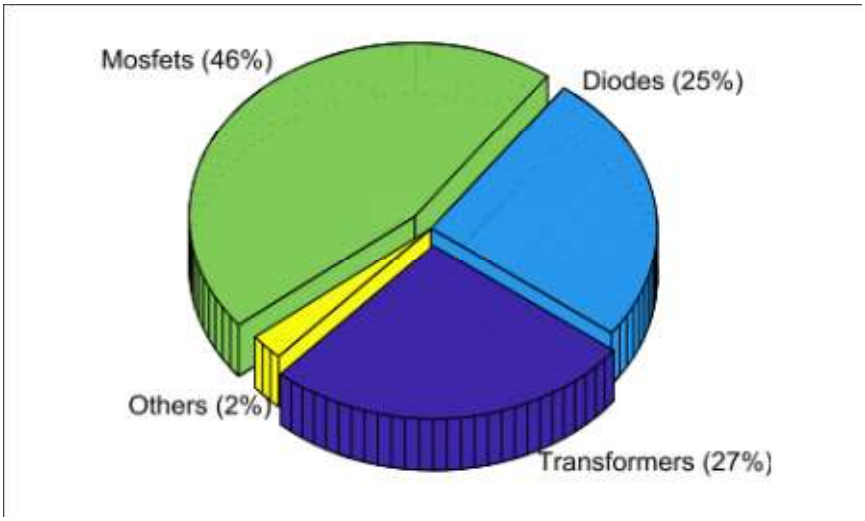

(b)

Fig. 5.12 Power of transformer's efficiency work in both mode (a) Charge mode

(b) Discharge mode

Chapter 6 Conclusion and Recommendation for Future Work

A new integrated four-port DC-DC converter which was able to regulate voltage and power is proposed for a hybrid energy system in this thesis. The proposed converter utilizes phase-shift control to adjust the PWM wave and is used for interfacing a hybrid system with different energy sources, including PV panel, WTG, and battery block. By building a small-signal model from equations, multiple controllers are developed to regulate the DC-link voltage, battery voltage, and current. The detail and theories about designing transfer and how to choose parameters were present in this thesis. With the developed prototye, simulation and experiment are carried out. The converter not only is capable of MPPT for the PV panel and WTG, but also can control charge and of the battery to maintain the DC-link voltage at a constant value.

To conclude, according to phase-shift control and MPPT, the new type of four-port DC converter was built with high-efficiency transformers, which is able to balance the three kinds of different power sources and output in a regulated level in this thesis. Furthermore, a new transformer design subject higher current and frequency. However, there are still space left to improve the quality and depth of this thesis, e.g., improving the efficiency of the transformer, considering the multi-direction trans, and increasing the circuit sensitivity.

Bibliography

[1] S. R. Bull, “Renewable energy today and tomorrow,” *Proc. IEEE*, 2001.

[2] J. Zeng, J. Ning, X. Du, T. Kim, Z. Yang, and V. Winstead, “A Four-port DC-DC Converter for a Standalone Wind and Solar Energy System,” *IEEE Trans. Ind. Appl.*, pp. 1–1, 2019.

[3] H. Wu, K. Sun, R. Chen, H. Hu, and Y. Xing, “Full-bridge three-port converters with wide input voltage range for renewable power systems,” *IEEE Trans. Power Electron.*, 2012.

[4] Z. Ding, C. Yang, Z. Zhang, C. Wang, and S. Xie, “A novel soft-switching multiport bidirectional dc-dc converter for hybrid energy storage system,” *IEEE Trans. Power Electron.*, 2014.

[5] Z. Qian, O. Abdel-Rahman, H. Al-Atrash, and I. Batarseh, “Modeling and control of three-port DC/DC converter interface for satellite applications,” *IEEE Trans. Power Electron.*, 2010.

[6] K. Itoh, M. Ishigaki, N. Yanagizawa, S. Tomura, and T. Umeno, “Analysis and design of a multi-port converter using a magnetic coupling inductor technique,” 2013.

[7] S. C. Bhattacharyya and S. C. Bhattacharyya, “Energy Access,” in *Energy Economics*, 2019.

[8] O. Cornea, G. D. Andreescu, N. Muntean, and D. Hulea, “Bidirectional Power Flow Control in a DC Microgrid Through a Switched-Capacitor Cell Hybrid DC-DC Converter,” *IEEE Trans. Ind. Electron.*, 2017.

[9] H. Wu, P. Xu, H. Hu, Z. Zhou, and Y. Xing, “Multiport converters based on integration of full-bridge and bidirectional DC-DC topologies for renewable generation systems,” *IEEE Trans. Ind. Electron.*, 2014.

[10] W. Short, “Renewable electricity,” in *Engineering Response to Climate Change, Second Edition*, 2013.

[11] F. Katiraei, M. R. Iravani, and P. W. Lehn, “Micro-grid autonomous operation during and subsequent to islanding process,” *IEEE Trans. Power Deliv.*, 2005.

[12] F. Mwasilu, J. J. Justo, E. K. Kim, T. D. Do, and J. W. Jung, “Electric vehicles and smart grid interaction: A review on vehicle to grid and renewable energy sources integration,” *Renewable and Sustainable Energy Reviews*. 2014.

[13] R. Priewasser, M. Agostinelli, C. Unterrieder, S. Marsili, and M. Huemer, “Modeling, control, and implementation of DC-DC converters for variable frequency operation,” *IEEE Trans. Power Electron.*, 2014.

[14] S. Y. Hui and H. S. H. Chung, “Resonant and soft-switching converters,” in *Power Electronics Handbook*, 2011.

[15] G. B. Koo, G. W. Moon, and M. J. Youn, “New zero-voltage-switching phase-shift full-bridge converter with low conduction losses,” *IEEE Trans. Ind. Electron.*, 2005.

[16] K. B. Park, C. E. Kim, G. W. Moon, and M. J. Youn, “Voltage oscillation reduction technique for phase-shift full-bridge converter,” *IEEE Trans. Ind. Electron.*, 2007.

[17] Z. Yan, Z. Zhang, J. Li, S. Xu, and L. Yang, “The Uni-Polarity Phase-Shifted

Modulation Strategy for Single-Phase High-Frequency Link Inverter Based on De-Re-Coupling Idea and Dead Time Optimization," *Diangong Jishu Xuebao/Transactions China Electrotech. Soc.*, 2018.

[18] W. Li, J. Xiao, Y. Zhao, and X. He, "PWM plus phase angle shift (PPAS) control scheme for combined multiport DC/DC converters," *IEEE Trans. Power Electron.*, 2012.

[19] J. Zeng, J. Ning, T. Kim, and V. Winstead, "Modeling and control of a four-port DC-DC converter for a hybrid energy system," 2019.

[20] M. Michon, J. L. Duarte, M. Hendrix, and M. G. Simões, "A three-port bi-directional converter for hybrid fuel cell systems," 2004.

[21] H. Al-Atrash, J. Reese, and I. Batarseh, "Tri-modal half-bridge converter for three-port interface," 2007.

[22] W. Li, Y. He, X. He, Y. Sun, F. Wang, and L. Ma, "Series asymmetrical half-bridge converters with voltage autobalance for high input-voltage applications," *IEEE Trans. Power Electron.*, 2013.

[23] F. Z. Peng, M. Shen, and K. Holland, "Application of Z-source inverter for traction drive of fuel cell-battery hybrid electric vehicles," *IEEE Trans. Power Electron.*, 2007.

[24] H. Al-Atrash and I. Batarseh, "Boost-integrated phase-shift full-bridge converter for three-port interface," 2007.

[25] G. P. Adam and B. W. Williams, "Half-and full-bridge modular multilevel converter models for simulations of full-scale HVDC links and multiterminal

DC grids," 2014.

[26] M. A. G. De Brito, L. Galotto, L. P. Sampaio, G. De Azevedo Melo, and C. A. Canesin, "Evaluation of the main MPPT techniques for photovoltaic applications," *IEEE Trans. Ind. Electron.*, 2013.

[27] M. Patty, *Electric transformer*. 1992.

[28] R. Prieto, J. A. Cobos, O. García, P. Alou, and J. Uceda, "Using parallel windings in planar magnetic components," 2001.

[29] I. W. Hofsajer, K. Fricker, and M. O. Crosato, "Reduction of EMI in planar transformers by charge balancing," *Electron. Lett.*, 2002.

[30] B. W. Carsten, "The low leakage inductance of planar transformers; fact or myth?," 2001.

[31] E. Mulasalihović, H. Pfützner, S. Traxler, and H. Yamaguchi, "Effects of geomagnetically induced currents on the magnetic performance of transformer cores," *J. Magn. Magn. Mater.*, 2008.

[32] C. Quinn, K. Rinne, T. O'Donnell, M. Duffy, and C. O. Mathúna, "A review of planar magnetic techniques and technologies," 2001.

[33] M. T. Quirke, J. J. Barrett, and M. Hayes, "Planar Magnetic Component Technology—A Review," *IEEE Trans. Components, Hybrids, Manuf. Technol.*, 1992.

[34] S. O'Reilly, M. Duffy, T. O'Donnell, S. C. Ó. Mathúna, M. Scott, and N. Young, "New integrated planar magnetic cores for inductors and transformers fabricated in MCM-L technology," *Adv. Microelectron.*, 2000.

[35] X. Huang, K. D. T. Ngo, and G. Bloom, “Design techniques for planar windings with low resistances,” 1995.

[36] G. Skutt, F. C. Lee, R. Ridley, and D. Nicol, “Leakage inductance and termination effects in a high-power planar magnetic structure,” 1994.

[37] D. Van Der Linde, C. A. M. Boon, and J. Ben Klaassens, “Design of a High-Frequency Planar Power Transformer in Multilayer Technology,” *IEEE Trans. Ind. Electron.*, 1991.

[38] W. G. Hurley, “Optimizing core and winding design in high frequency transformers,” *Int. Power Electron. Congr. - CIEP*, 1996.

[39] W. G. Hurley, E. Gath, and J. G. Breslin, “Optimizing the AC resistance of multilayer transformer windings with arbitrary current waveforms,” *IEEE Trans. Power Electron.*, 2000.

[40] G. E. Evaluation and B. User, “GS66508B-EVBDB1 GaN E-HEMT Daughter Board and GS665MB-EVB Evaluation Platform User ’ s Guide GS66508B-EVBDB1,” pp. 1–31.

[41] W. Li, C. Xu, H. Luo, Y. Hu, X. He, and C. Xia, “Decoupling-Controlled Triport Composited DC/DC Converter for Multiple Energy Interface,” *IEEE Trans. Ind. Electron.*, 2015.

Refereed Journal Papers

[J1] Jianwu Zeng, Jiahong Ning, Xia Du, Taesic Kim, Zhaoxia Yang, and Vincent Winstead, "A Four-port DC-DC Converter for a Standalone Wind and Solar Energy System" IEEE Transactions on Industry Application (TIA), 10.1109/TIA.2019.2948125, Oct 2019.

Refereed Conference/Poster Papers

[C1] Xia Du, Jiahong Ningand Jianwu Zeng, "Modeling and Control of a Four-Port Bidirectional DC-DC Converter for a DC Microgrid with Renewable Energy Sources" IEEE Applied Power Electronic Conference and Exposition, New Orleans, Mar, 2020. pp. 3391-3396.

[C2] Jiahong Ning, Jianwu Zeng and Xia Du, "A Four-port Bidirectional DC-DC Converter for Renewable Energy-BatteryDC Microgrid System" IEEE ECCE — IEEE Energy Conversion Congress and Exposition, Baltimore, USA, Oct, 2019. (Oral Presentation).

[C3] Jianwu Zeng, Jiahong Ning, Taesic Kim, and Vincent Winstead "Modeling and Control of a Four-port DC-DC Converter for a Hybride Energy System" IEEE APEC — IEEE Applied Power Electronic Conference and Exposition, Los angeles, USA, Mar, 2019.(Oral presentation).

[C4] Dianzhi Yu, Jianwu Zeng, Junhui Zhao and Jiahong Ning, "A Two-stage Four-port Inverter for Hybride Renewable Energy System Integration" IEEE APEC — IEEE Applied Power Electronic Conference and Exposition, Losangle, USA, Mar, 2019.(Poster).

Appendix

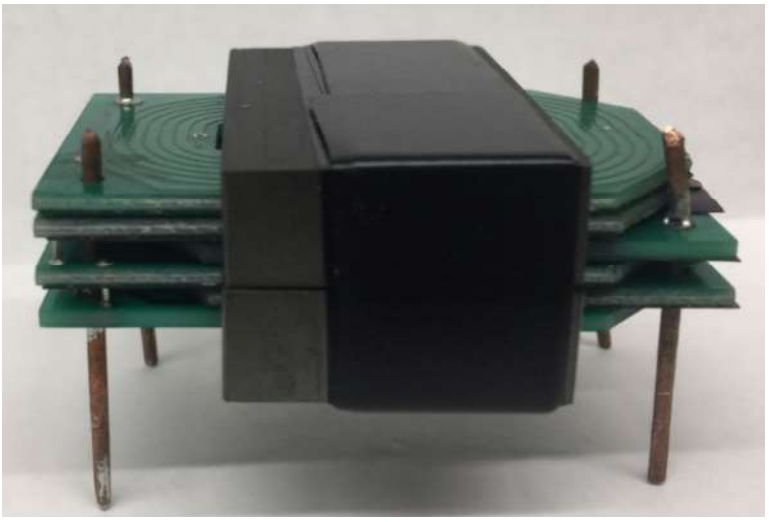

(a)

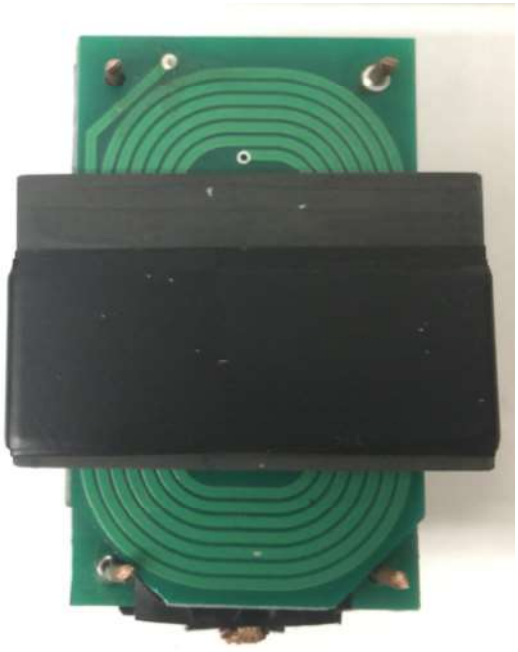

(b)

A. 1 Physical transformer(a) Side view (b)Overlook view

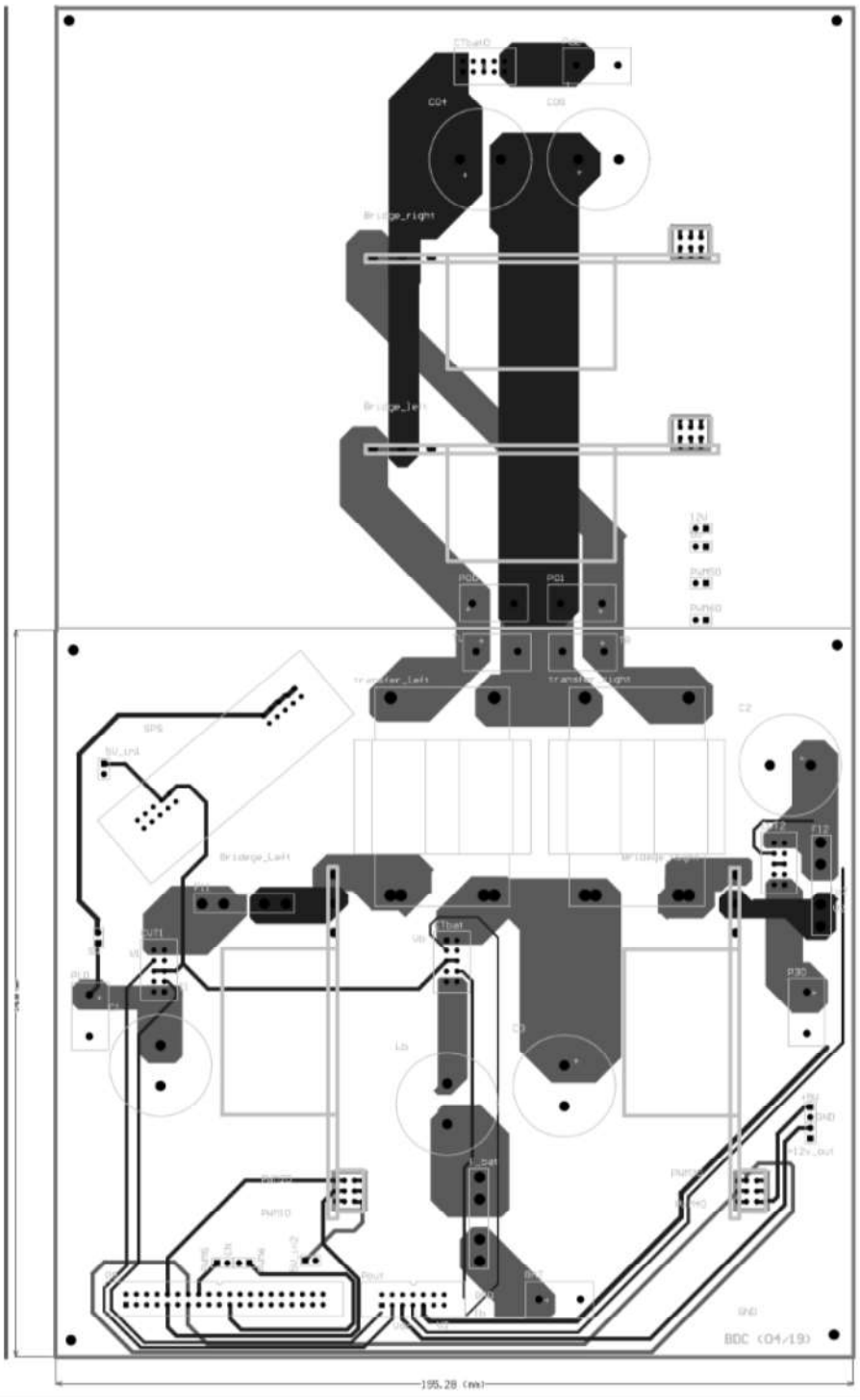

A. 2 PCB layout schematic page